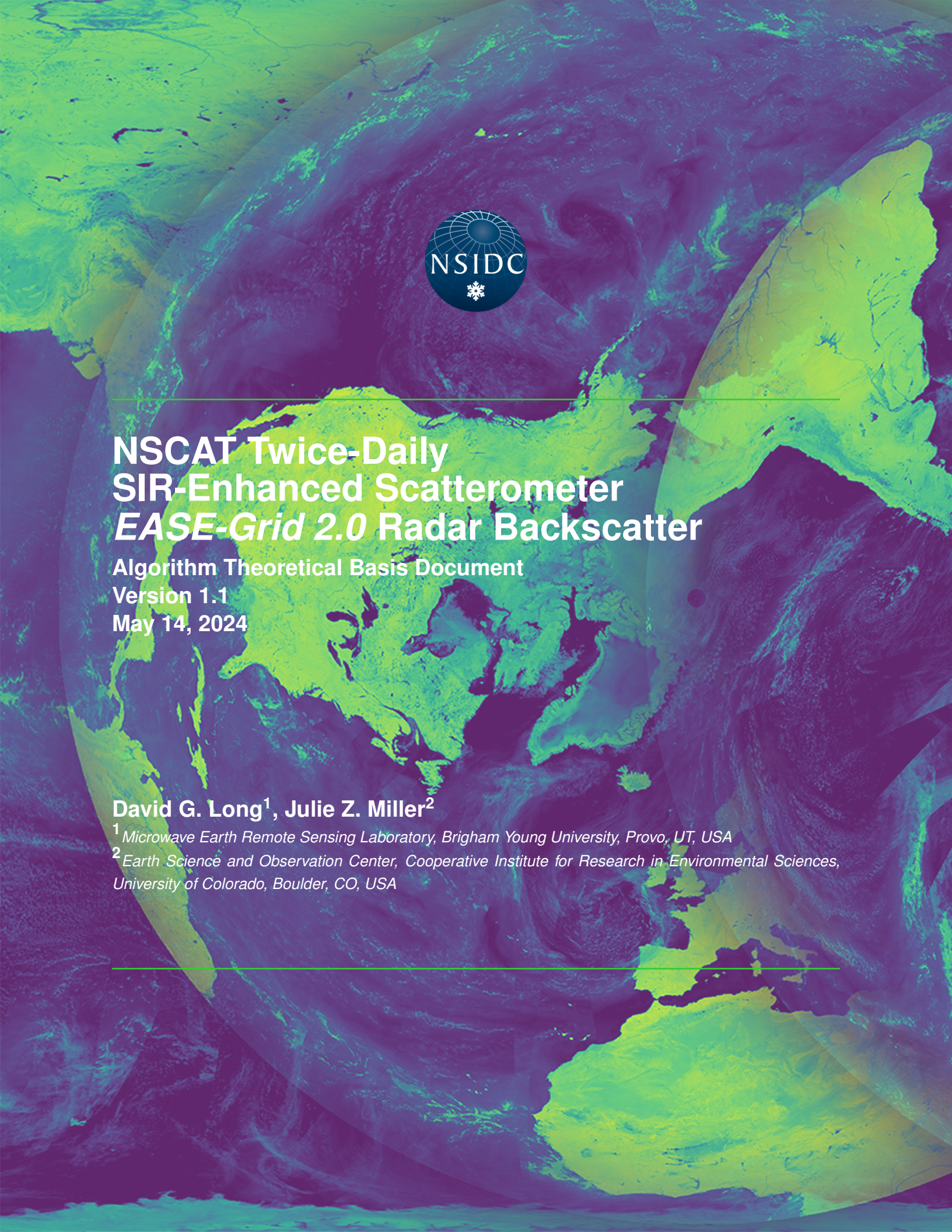

# NSCAT Twice-Daily SIR-Enhanced Scatterometer *EASE-Grid 2.0* Radar Backscatter

## Algorithm Theoretical Basis Document

**Version 1.1**

**May 14, 2024**


**David G. Long[1], Julie Z. Miller[2]**

[1] *Microwave Earth Remote Sensing Laboratory, Brigham Young University, Provo, UT, USA*

[2] *Earth Science and Observation Center, Cooperative Institute for Research in Environmental Sciences, University of Colorado, Boulder, CO, USA*

*Cover Image*
Color montage of morning overpass AMSR2 horizontally-polarized 36 GHz passive microwave brightness temperatures, 29–30 June, 2003, by M. J. Brodzik, National Snow and Ice Data Center.

*Citation*
David G. Long and Julie Z. Miller. 2024. NSCAT Twice-Daily SIR-Enhanced Scatterometer EASE-Grid 2.0 Radar Backscatter Algorithm Theoretical Basis Document, Version 1.0. NSIDC White Paper. https://doi.org/TBD.

# Contents

# List of Figures

# List of Tables

# 1 Revision History

**Table 1:** *ATBD Revision History*

| Revision | Date | Purpose |
|---|---|---|
| 1.0 | 2023-01-05 | Initial Version |
| 1.1 | 2023-06-03 | Update information azimuth products |

**Table 2:** *Data Set Revision History*

| Revision | Date | Purpose |
|---|---|---|
| 1.0 | 2023-01-05 | Initial Data Release |

# 2 Acronyms and Abbreviations

**Table 3:** *List of Acronyms and Abbreviations*

| | |
|---|---|
| ADEOS | Advanced Earth Observing Satellite |
| ATBD | Algorithm Theoretical Basis Document |
| AVE | weighted AVEraging image formation algorithm |
| bSIR | Scatterometer Image Reconstruction using binary response function |
| BYU | Brigham Young University |
| CDR | Climate Data Record |
| CETB | Calibrated Passive Microwave Daily EASE-Grid 2.0 Brightness Temperature |
| CF | Climate and Forecast Metadata Conventions |
| DAAC | Distributed Active Archive Center |
| dB | decibel ($10\log_{10}$) |
| DDP | Digitial Doppler Processor |
| DIB | Drop-In-the-Bucket averaging (used to produce GRD products) |
| DOY | Day Of Year |
| E2N | EASE-Grid 2.0, Northern Hemisphere Projection |
| E2S | EASE-Grid 2.0, Southern Hemisphere Projection |
| E2T | EASE-Grid 2.0, Temperate and Tropical Cylindrical Projection |
| EASE-Grid | Equal-Area Scalable Earth Grid (Original Definition) |
| EASE-Grid 2.0 | Equal-Area Scalable Earth Grid Version 2.0 |
| EASE2-M | EASE-Grid 2.0, Mid- and Low-Latitude Cylindrical Projection |
| EASE2-N | EASE-Grid 2.0, Northern Hemisphere Projection |
| EASE2-S | EASE-Grid 2.0, Southern Hemisphere Projection |
| EASE2-T | EASE-Grid 2.0, Temperate and Tropical Cylindrical Projection |
| EIA | Earth Incidence Angle |
| EOSDIS | Earth Observing System Data and Information System |
| ESDR | Earth System Data Record |
| FA | incidence-angle Fixed Azimuth modulation coefficients |
| FCDR | Fundamental Climate Data Record |
| GHz | GigaHertz |
| GRD | (Drop-In-the-Bucket) Gridding Method |
| HH | Horizontal-polarization transmit, Horizontal-polarization receive |
| HV | Horizontal-polarization transmit, Vertical-polarization receive |
| ltod | local-time-of-day |
| MEaSUREs | Making Earth System Data Records for Use in Research Environments |
| MHz | MegaHertz |
| MRF | Measurement Response Function |

| | |
|---|---|
| NASA | National Aeronautics and Space Administration |
| NSCAT | NASA Scatterometer |
| NOAA | National Oceanic and Atmospheric Administration |
| NORAD | North American Aerospace Defense Command |
| NSIDC | National Snow and Ice Data Center |
| NetCDF | Network Common Data Format |
| PRF | Pulse Repetition Frequency |
| PSRF | Pixel Spatial Response Function |
| rSIR | radiometer version of SIR |
| SAR | Synthetic Aperture Radar |
| SASS | Seasat Scatterometer |
| SCP | Scatterometer Climate Record Pathfinder |
| SDR | Sensor Data Record |
| Sigma-0 | normalized radar cross section or backscatter ($\sigma^o$) |
| SIR | Scatterometer Image Reconstruction |
| TBD | To Be Determined |
| TLE | Two-Line Element |
| UTC | Coordinated Universal Time |
| VA | incidence-angle Variable Azimuth modulation coefficients |
| VH | Vertical-polarization transmit, Horizontal-polarization receive |
| VV | Vertical-polarization transmit, Vertical-polarization receive |
| XX | Cross-polarization (mean of HV and VH values) |

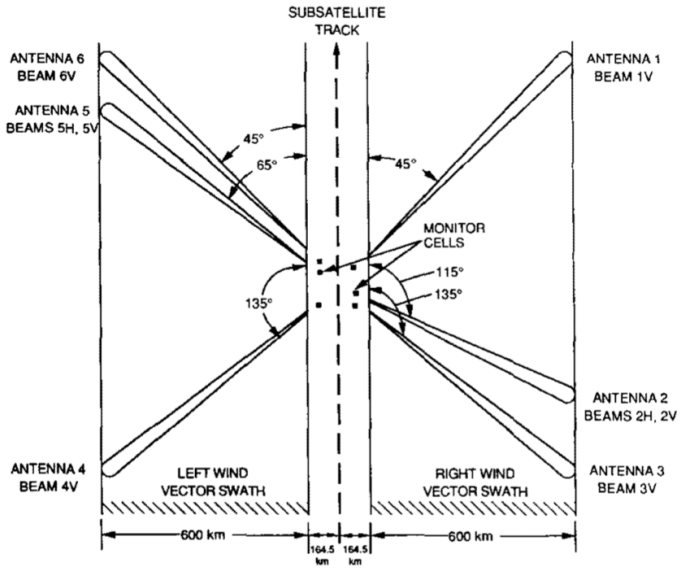


**Figure 1:** *NSCAT observation swath. Nominally 25 km $\sigma^o$ measurements are collected over two 750 km swaths separated by a nadir gap. Measurements are not collected over the central (nadir) gap (Long et al., 2019).*

# 3 Purpose of this Document

This documents describes the CETB-compatible radar backscatter product "NSCAT Scatterometer Twice-Daily SIR-Enhanced EASE-Grid 2.0 Radar Backscatter", (NSIDC-0786, doi:10.5067/APSWI5NK3PKJ) created from 14 GHz NASA Scatterometer (NSCAT) observations collected during the NSCAT mission in 1996-1997.

NSCAT collected nominally 25 km resolution normalized radar cross section ($\sigma^o$) from 6 different azimuth angles over two 600 km wide swaths with a 300 km gap. Two of the antennas were dual-polarized (Graf et al., 1998). NSCAT employed long, fan-beam antennas with narrow ($\sim$ 7 km) narrow beamwidths, see Fig. 1. Along-beam resolution was achieved using 5 ms continuous wave (CW) transmit pulses and multiple bandpass filters, implemented in a digital doppler processor (DDP), to achieve along-beam resolution via band pass filtering the of the echo. By varying the parameters of the DDP bandpass filters, the DDP maintained the measurement areas at fixed cross-track distances from the spacecraft nadir track, which overcame a key limitation of the Seasat scatterometer (SASS) (Long et al., 1988). The multiple beams provided azimuth diversity of the $\sigma^o$ measurements, which is required to retrieve the surface wind (Ulaby and Long, 2014)(Naderi et al., 1991).

While designed and optimized for ocean observation, NSCAT also collected $\sigma^o$ measurements over land and ice. The observed $\sigma^o$ depends on the surface roughness, geometry, and dielectric constant. These depend on geophysical parameters of interest such as surface

freeze/thaw state, snow and ice structure, moisture content, and vegetation characteristics, among others (Ulaby and Long, 2014). The NSCAT data set provides a unique "snapshot" of the Earth during its mission lifetime.

The NSCAT radar backscatter (*NSCAT*) product exploits the NSCAT measurements to create a unique backscatter image data set that captures the state of the Earth during the NSCAT mission (1996-1997). To exploit this data, we employ image reconstruction techniques to create daily and twice-daily conventional resolution and enhanced resolution NSCAT radar images from the measurements. The new data set is provided to the science community to support cryosphere and climate studies.

# 4 Gridded and SIR-Enhanced Product Description

## 4.1 Product Description

The *NSCAT* product includes Level 1 gridded, twice-daily, radar backscatter data collected at 13.995 GHz for two radar channels (horizontal transmit-horizontal receive [HH] and vertical transmit-vertical receive [VV]. Data are gridded to the EASE-Grid 2.0 Azimuthal and Cylindrical projections (Brodzik et al., 2012)(Brodzik et al., 2014), at two spatial resolutions, as described below. The *NSCAT* product is archived and distributed by the National Snow and Ice Data Center Distributed Active Archive Center (`https://nsidc.org/data/NSIDC-TBD/versions/1`).

Input data for the *NSCAT* v1.0 product are the NSCAT L1.5 Sigma0 files (Faist and Lee, 1997). Using the quality flags in the input data, only the highest quality measurements are included in *NSCAT* product. The data coverage is global for the period beginning 14 Sept 1996 (DOY 258) through 28 June 1997 (DOY 179). No calibration corrections were applied to the data (Tsai et al., 1999).

## 4.2 NSCAT Instrument

NSCAT flew as an attached payload on the Advanced Earth Observing Satellite (ADEOS) spacecraft, which was launched on 17 Aug 1996 from the Tanegashima Space Center, Japan and operated for approximately 9 months before the spacecraft power system failed due a detached solar array. ADEOS flew in a sun-synchronous 800 km circular polar orbit with an orbit inclination angle of 98.7° and a 10:30 AM local descending orbit equator crossing.

The NSCAT instrument is described in Naderi et al. (1991), JPL (1997) with more detail on the DDP in Long et al. (1988). NSCAT is a fan-beam Doppler scatterometer (Ulaby and Long, 2014), like its predecessor the SASS (Grantham et al., 1977), though with a DDP instead of analog filters.

The NSCAT instrument employed six 3 m long fan-beam antennas deployed to provide three azimuth angle observations on each side of the spacecraft. The center antenna operated in dual polarization (HH and VV), while the other antennas used only VV polarization, see Fig. 1. Along-track resolution was provided by the narrow beamwidth of the antenna beams and the pulse timing. Along-beam resolution was provided via Doppler filtering, see Fig. 2.

The return echo was Doppler filtered using the DDP into 25 measurement “cells”, one of which was designated the “monitor cell” and was adjusted to make measurements at a fixed 11° incidence angle. The Doppler center frequency and bandwidth of the other cells were adjusted to maintain the cells at a fixed cross-track distance from the spacecraft ground track throughout the orbit. The NSCAT swath and measurement geometry (Fig. 2) produced a 4-sided instantaneous 3-dB footprint for each pulse. A total of 25 sequential

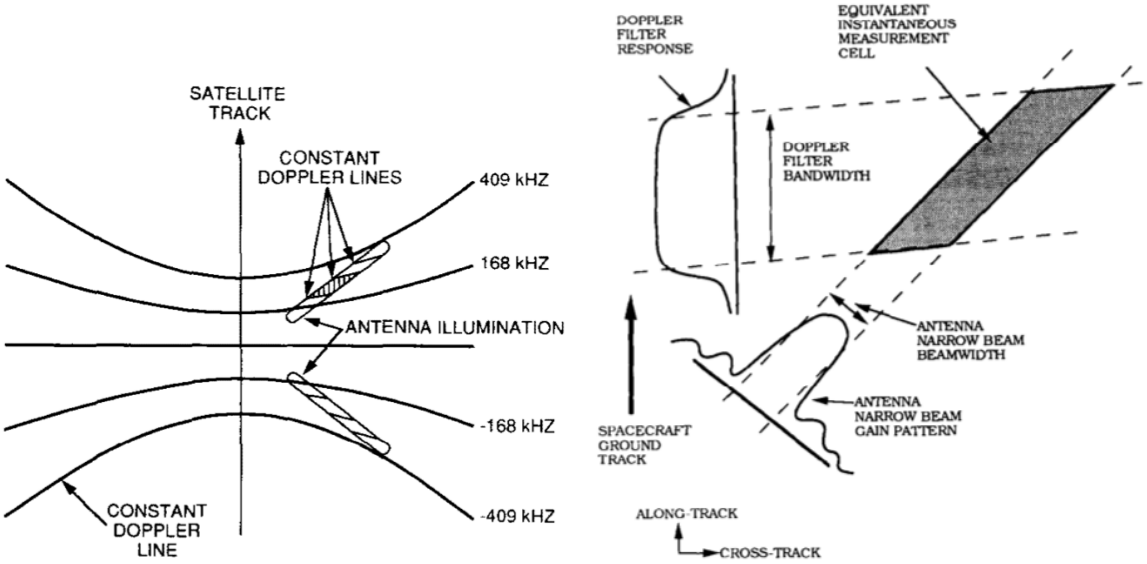


**Figure 2:** *NSCAT measurement theory illustrations. (left) Intersection of the fan-beam footprint and iso-Doppler lines used to define the along-beam resolution. (right) Antenna pattern and Doppler filtering that define the individual $\sigma^o$ measurement footprints for a forward-facing antenna.*

pulses were issued on each of the 8 beams in sequence during the time it takes for the spacecraft to travel 25 km resulting in an along-track spacing of 25 km between along-track measurements from the same azimuth angle (Naderi et al., 1991)(Long et al., 1988).

The 25 pulses were processed and summed into a single measurement. As shown in Fig. 3, this produces six-sided 3-dB footprints on the surface. Assigning 1 to areas within the 3-dB footprint and 0 outside results in a simplified *binary* description of the measurement's MRF. The *full response* includes the filter and antenna pattern rolloff. The full response minimizes coverage gaps, but is slightly smoother than the binary response when used in SIR or AVE. Examples of the full response for several NSCAT measurements are illustrated in Fig. 4. Image examples based on the full response and the binary response are shown in Section 6. Further comparisons of the full and binary responses are provided in Section 6.3.

Note that while a radiometer's footprint is defined by the antenna pattern, the radar footprint is defined by the antenna pattern squared due to the two-way travel of the signal from radar to the surface (Ulaby and Long, 2014).

NSCAT collected return echo power measurements, which were converted into $\sigma^o$ using the radar equation (JPL, 1997)(Ulaby and Long, 2014). The nominal resolution of these measurements is described as 25 km, though the effective resolution varies over the swath and orbit. The $\sigma^o$ value depends on the surface roughness, geometry, and dielectric constant (Ulaby and Long, 2014).

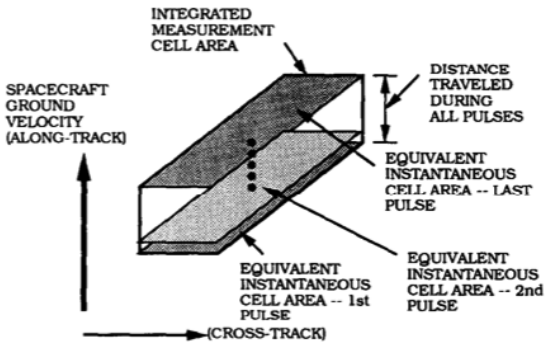


**Figure 3:** *Illustration of the footprint when integrating multiple pulses into a single measurement (Long et al., 1993).*

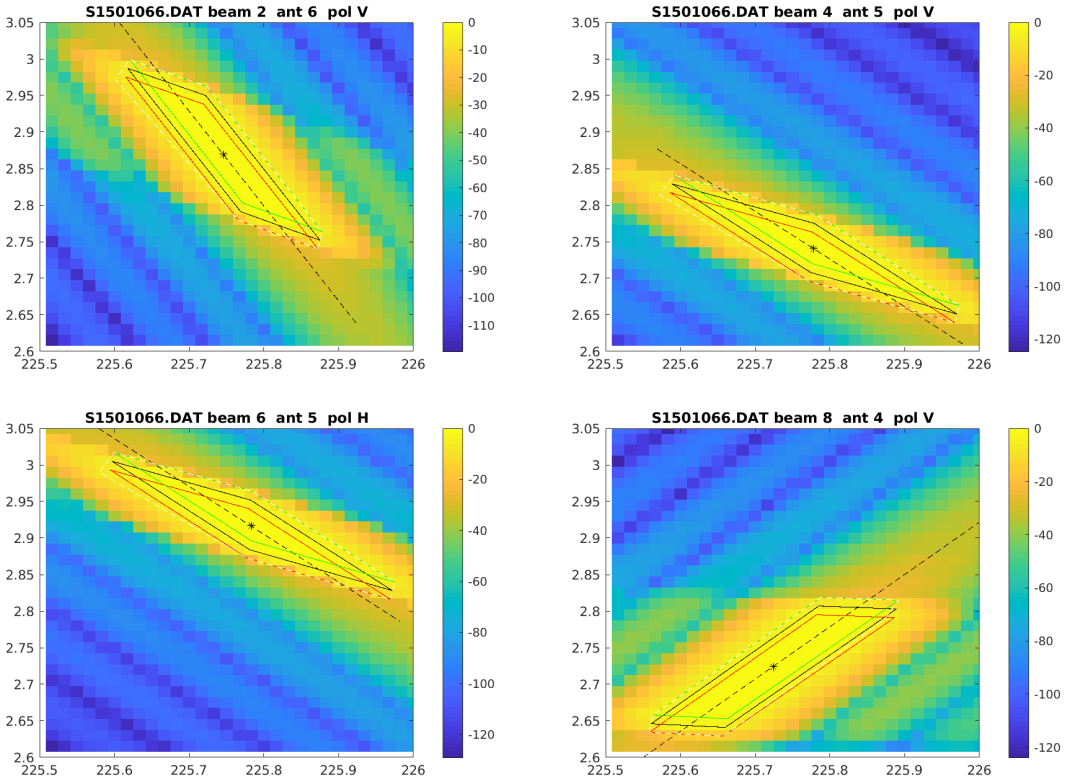


**Figure 4:** *Arbitrarily selected examples of the full spatial gain pattern response of several mid-swath NSCAT $\sigma^o$ measurements from different antenna beams. The dashed line shows the along-beam direction. The red, black, and green quadrilaterals show the instantaneous 3-dB footprint for the first, twelfth, and twenty-fifth pulses.*

To better understand the spatial layout of the NSCAT $\sigma^o$ measurements, Figs. 5–8 are presented. Figure 5 shows the positions of the centers of all the $\sigma^o$ measurements from a single orbit pass. Preceding and succeeding orbits have a similar pattern, but are horizontally shifted. Figure 6 (left) shows the footprint locations for one beam cycle during an ascending orbit, while Figure 6 (right) shows the measurement centers for one side of a descending pass. Figures 7 and 8 show further zoom ins for each beam separately.

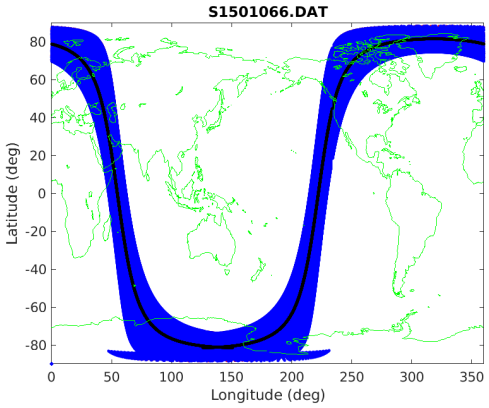


**Figure 5:** *NSCAT $\sigma^o$ measurement locations during a single orbit. Individual measurements cannot be resolved in this plot.*

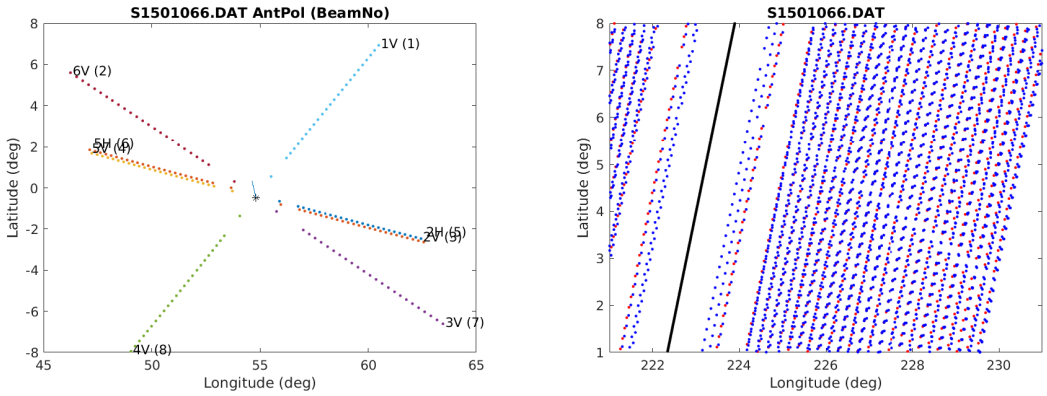


**Figure 6:** *NSCAT $\sigma^o$ measurement locations (left) for a particular antenna cycle during an ascending pass, and (right) for multiple pulse cycles zoomed in during a descending pass. Note that the center antennas are dual-polarization. The diagonal patterns are the result of missing $\sigma^o$ measurements due to a calibration cycle, which occurs once per 100 antenna cycles. Each antenna beam is a different color.*

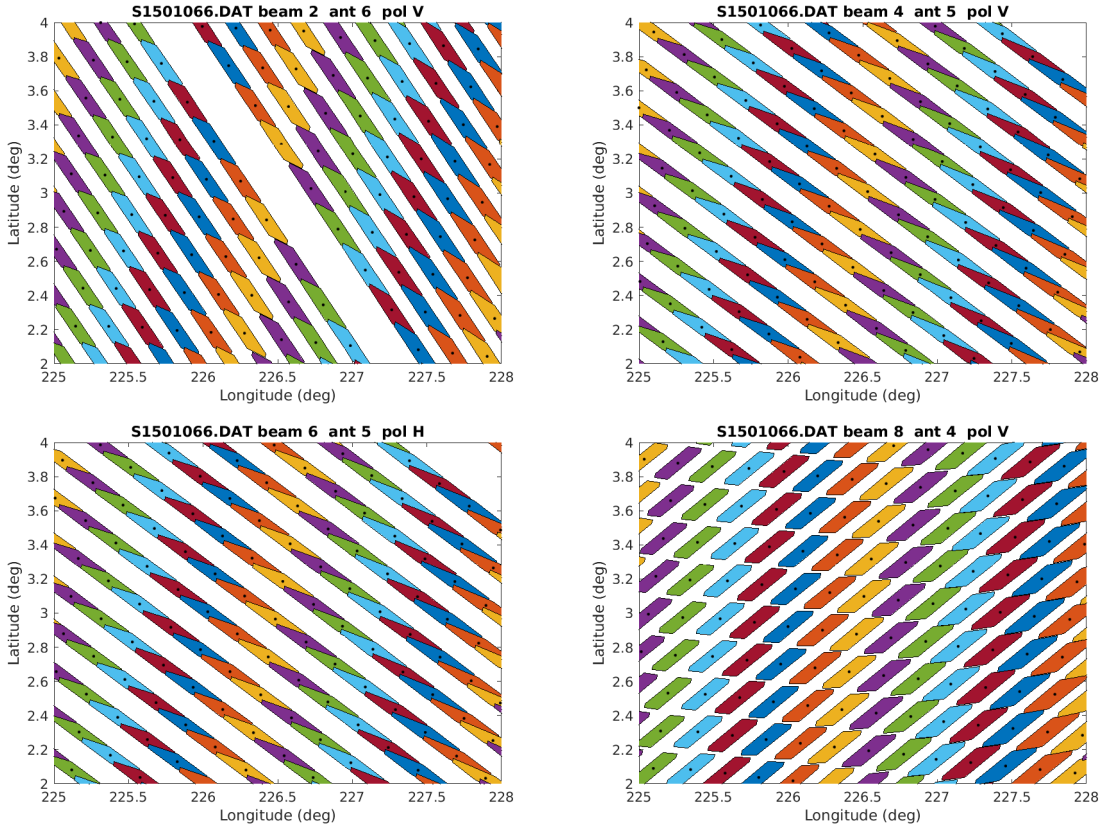


**Figure 7:** *NSCAT 3-dB $\sigma^o$ measurement layouts for each beam. This is a zoom in of Fig. 6. Colors correspond to the along-beam measurement number. So, a particular color is a fixed cross-track distance from the spacecraft nadir track. These represent the binary response function.*

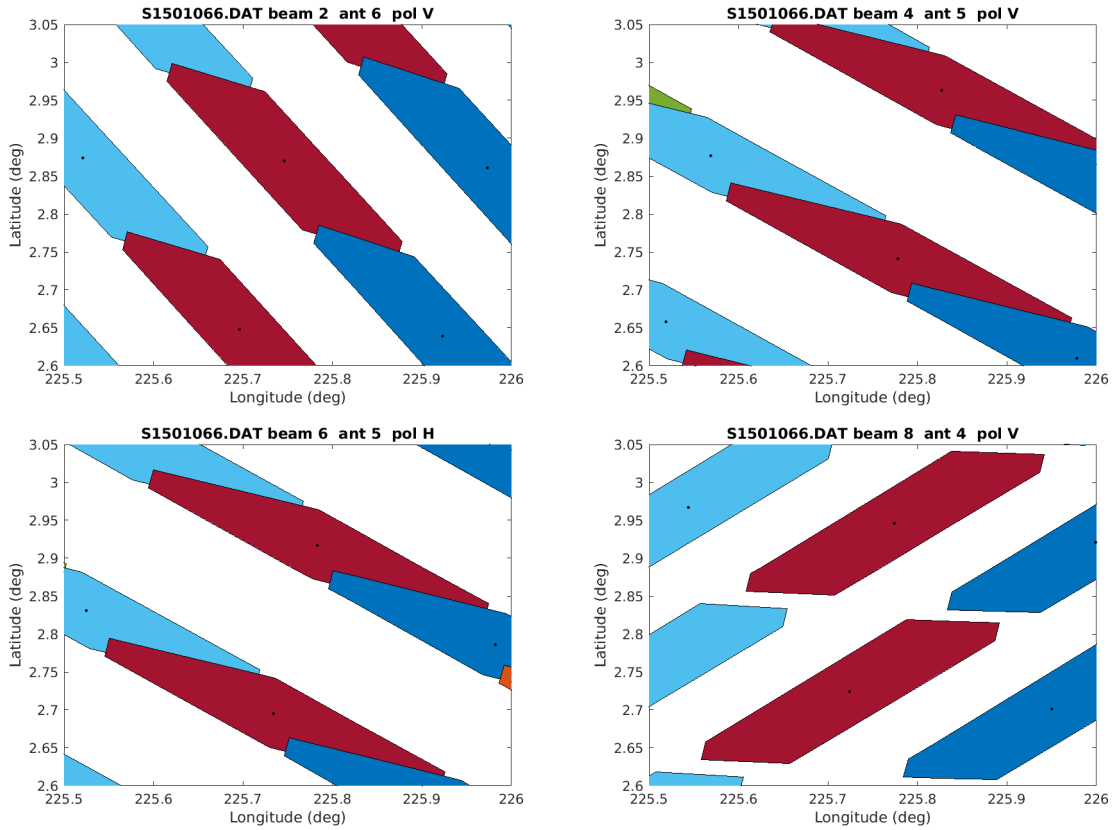


**Figure 8:** *NSCAT 3-dB $\sigma^o$ measurement layouts for each beam. This is a zoom in of Fig. 7. Colors correspond to the along-beam measurement number. So, a particular color is a fixed cross-track distance from the spacecraft nadir track. These represent the binary response function.*

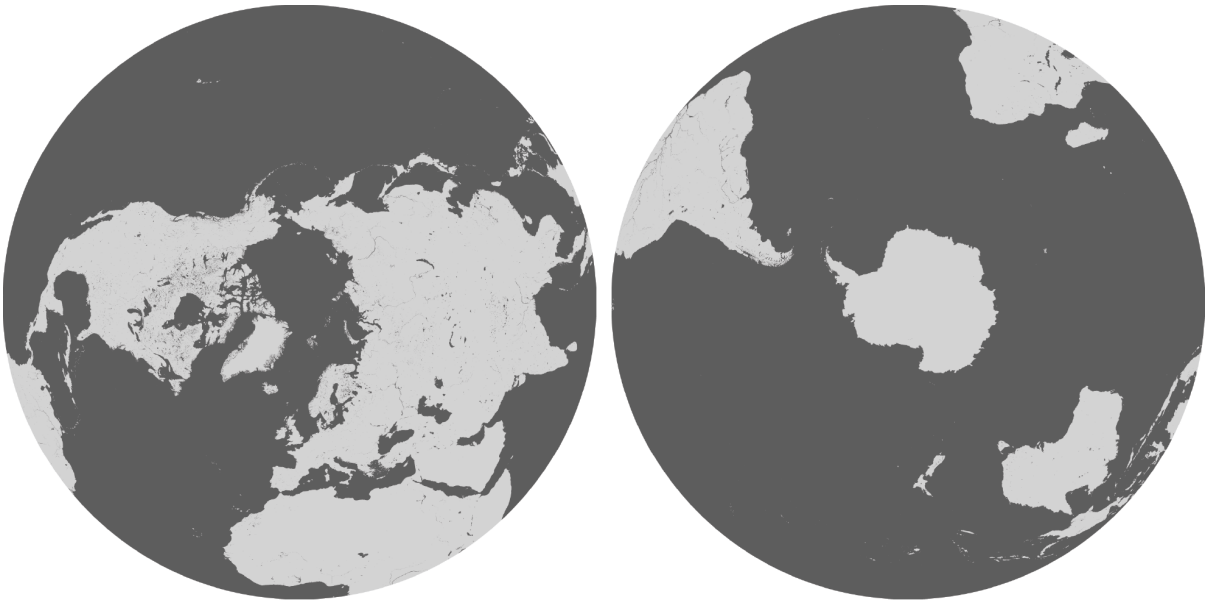

**Figure 9:** *Northern and Southern EASE-Grid 2.0 projection extents. The land-ocean mask from Brodzik and Knowles (2011).*

The ADEOS spacecraft flew in a sun-synchronous circular polar orbit at an inclination of $98.7°$ and an altitude of $900\,\mathrm{km}$ (JPL, 1997). During its mission lifetime, it had a 41 day exact repeat orbit and a 4 day near-repeat orbit, collecting $\sigma^o$ measurements essentially continuously on both sides of the spacecraft ground track[1]. As described below, from these $\sigma^o$ measurements twice-daily global images were created by (1) DIB gridding of the $\sigma^o$ measurements on a 25 km grid and (2) applying the SIR algorithm to enhance the effective resolution of the data by exploiting the irregular patterns of measurement locations and signal oversampling (from overlaps in adjacent footprints and overlapping swaths). The SIR images are reported on a 3.125 km grid.

## 4.3 Grid Spatial Extent

Azimuthal *NSCAT* grids extend to the full Northern (EASE2-N) and Southern (EASE2-S) hemispheres (Fig. 9), as described in Brodzik et al. (2012, 2014). The spatial extent of the equal-area cylindrical projections (Fig. 10 and Fig. 11) is defined to match the extent of compatible grids favored by two user communities: (1) the Mid-Latitude (EASE2-M) grid, extending to $\pm 85.044\,566\,4°$ latitude, has been adopted by the SMAP user community. And, (2) the Temperate and Tropical (EASE2-T) grid, limited to latitudes equatorward of

[1]A ground station was employed in New Mexico. During part of the mission, the instrument operation mode was altered over this area to optimize data collection at the ground station.

**Figure 10:** *Cylindrical EASE-Grid 2.0 projection extents. Full extent coverage is EASE2-M, with horizontal red lines delineating the smaller latitudinal extent of the EASE2-T grid. The land-ocean mask is from Brodzik and Knowles (2011).*

$\pm 67.1°$, is consistent with the original CETB products defined for similar scanning radiometers (Brodzik et al., 2021). See Appendix A Table 7 for grid specifications.

## 4.4 Grid Spatial Resolution

*NSCAT* grid resolutions are defined relative to a $25\,\mathrm{km}$ base resolution, i.e., $25\,\mathrm{km}$ and $3.125\,\mathrm{km}$ MEaSUREs CETB data products (Brodzik et al., 2021). Nested resolutions relative to the CETB $25\,\mathrm{km}$ base grids are defined using exact divisors of $2$, as illustrated in Figure 12. *NSCAT* projection extents, dimensions and grid cell size details are included in Appendix A. Grids used for *NSCAT* processing are included in Table 4.

**Table 4:** NSCAT *EASE-Grid 2.0 base grids produced by the projection and reconstruction algorithm. See Section 5 for GRD and SIR reconstruction details.*

| EASE2-M | EASE2-N | EASE2-S | EASE2-T |
|---|---|---|---|
| n/a | 25km (GRD) | 25km (GRD) | 25km (GRD) |
| n/a | 3.125km (GRD/SIR) | 3.125km (GRD/SIR) | 3.125km (GRD/SIR) |

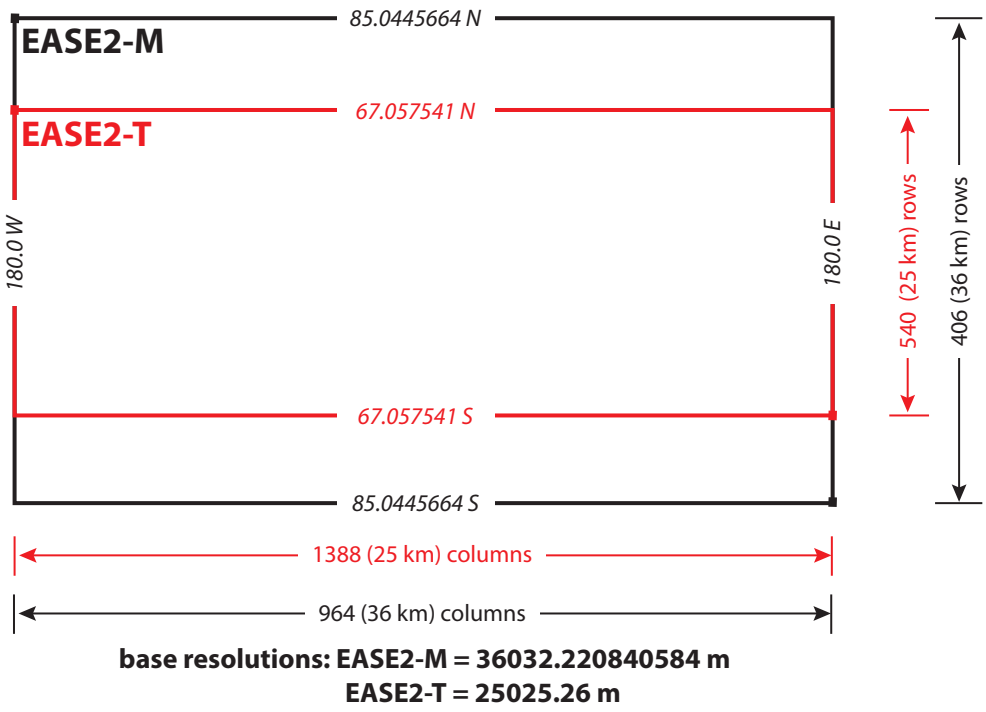


**Figure 11:** *Relationship of EASE-Grid 2.0 cylindrical projection extents. The EASE2-T extent is defined for compatibility with the CETB products. (Difference in latitudinal extent is exaggerated, see Fig. 10 for actual difference in projected extent (Brodzik et al., 2021).*

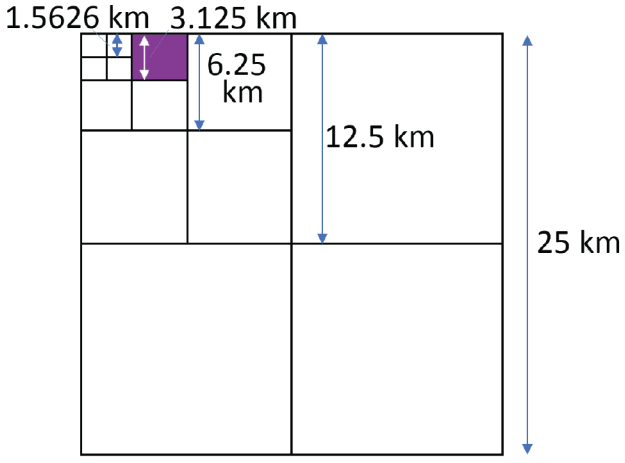


**Figure 12:** *CETB nested grids based on a 25 km base resolution. Only 25 km and 3.125 km divisions are used in* NSCAT *products (Long et al., 2019).*

## 4.5 Data Products

The *NSCAT* product at the NSIDC DAAC covers the period beginning 14 Sept 1996 (DOY 258) through 28 June 1997 (DOY 179). No calibration corrections were applied to the data. In creating a time series, a "moving average" approach was used with overlapping imaging periods that start every mission day and extend through the desired 4- or 8-day period (or to the end of the mission, whichever comes first). Table 5 summarizes the available *NSCAT* products, which are all in CETB-standard EASE-2 Grid projections.

**Table 5:** *Available twice-daily NSCAT image products.*

| MRF Type | days | Algo-rithm | Pix. Res. (km) | Regions* | Polar-ations | Size† N/S/T (MB) |
|---|---|---|---|---|---|---|
| | 4,8 | GRD | 25 | N,S,T | HH,VV | 6/6/9 |
| Binary | 4,8 | SIR | 3.125 | N,S,T | HH,VV | 531/531/768 |
| Full | 4,8 | SIR | 3.125 | N,S,T | HH,VV | 531/531/768 |

∗ Region code: N=Northern Hemisphere, S=Southern Hemisphere, T=Global
† Uncompressed size

# 5 Algorithm Description

## 5.1 Background

The *effective resolution* of an image is defined by the *pixel spatial response function* (PSRF), where the effective resolution is given by the dimension(s) of the one-half power (3-dB) extent of the PSRF. In contrast, the *measurement response function* (MRF) describes the spatial characteristics of the *individual* measurements. For a radar, the MRF depends on the two-way antenna gain pattern, the scan geometry, and the signal processing. For both radars and radiometers, the PSRF depends on the MRF and the image formation algorithm. In a linear image formation algorithm, the reported pixel value consists of the weighted sum of nearby measurements. In this case the PSRF is then the normalized weighted sum of the measurement MRF functions, including their spatial offset from the center of the pixel.

The spacing of pixels is termed the "pixel posting" or the "posting resolution". In creating the *NSCAT* backscatter image product, multiple measurements from different passes are combined into single pixel values. The resulting image pixels have an effective resolution slightly coarser than the posting resolution since (1) the measurements are not all centered the same, and (2) their MRFs can extend outside of the pixel area. The PSRF provides the tool for defining the effective pixel resolution (Long and Brodzik, 2016a). In order to be compatible with the CETB data set, two posting resolutions are considered: 25 km and 3.125 km, see Fig. 13.

## 5.2 *NSCAT* Backscatter Image Products

The *NSCAT* backscatter products include both low-noise (low-resolution) coarse resolution GRD images and higher-noise (enhanced) fine-resolution (SIR) images. The various products have their advantages and disadvantages. Multiple image types allow users the flexibility of choosing the appropriate images for their research application.

To create radar CETB-compatible products, different approaches are used for each resolution. Because the sensor was not designed as an imager, there are gaps between the measurements that must be filled by combining multiple passes over an extended imaging period. As a result of the 4 day near-repeat cycle, two imaging periods are defined: 4 day and 8 day to provide a user-selectable tradeoff between temporal resolution, spatial resolution, and noise.

For GRD images, the source backscatter measurements are gridded onto a 25 km grid using DIB techniques. In this approach, all the measurements whose center location falls within a grid element are averaged into the reported value. For the 3.125 km product, the source measurements are processed using the he first iteration of the SIR algorithm (AVE). AVE images use weighted averages where the weighting is the measurement MRF, which may vary from measurement to measurement. Along with each measurement's MRF, the

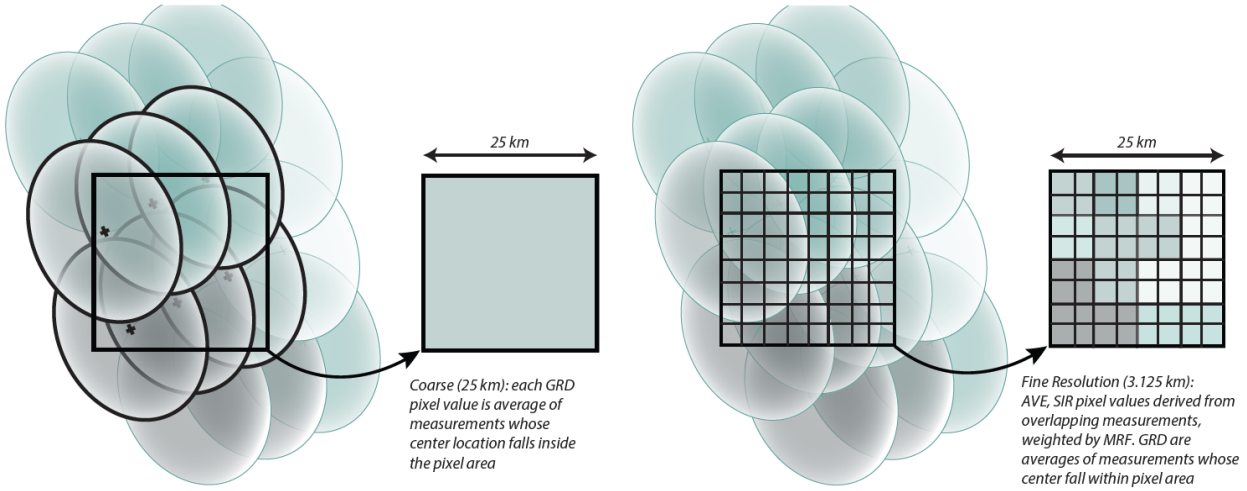


**Figure 13:** *Conceptual illustration of coarse 25 km (left) vs. high resolution 3.125 km (right) pixels. The ellipses represent the individual MRFs of the measurements (the actual shapes are more complicated than this.) DIB is used for GRD images while AVE and SIR are used for high resolution images.*

SIR algorithm exploits the irregular patterns of the measurement locations and signal oversampling from overlaps in adjacent footprints and overlapping passes. Table 5 summarizes the image product types.

## 5.3 Radar Spatial Response and Image Reconstruction

The effective spatial resolution of an image product is determined by the MRF of the sensor and by the image formation algorithm used. As previously noted, the MRF is determined by the antenna gain pattern, the scan geometry (notably the antenna scan angle), and the signal processing, see Long et al. (1993), Long (2017). The goal in forming a $\sigma^o$ image is to estimate the backscatter properties of the surface from noisy measurements that employ (possibly variable) MRFs that sample the surface. Though simple to implement, DIB techniques ignore the MRF, which limits their effective resolution. Reconstruction techniques that use the MRF can provide much finer effective resolution.

Reconstruction processing techniques effectively assume the underlying signal (the backscatter) being sampled is band-limited, which is the only consistent assumption possible with sampled data (Long and Brodzik, 2016b, Long and Franz, 2016b). For reconstruction, the backscatter at each point of a fine-scale pixel grid is estimated, producing a backscatter image or map. While the image is generated on a regular grid, the measurement locations and MRF are not aligned with the grid, and so the measurements form an irregular sampling pattern, which can complicate signal reconstruction. Many commonly used image formation algorithms either ignore this (as is done in DIB) or attempt to interpolate or

distance-weight the measurements values. In using image reconstruction, we avoid these ad hoc, non-optimal approaches and explicitly compute the MRF of each measurement as part of the reconstruction process. This is computationally intense, but provides the best possible image construction. The remainder of this section outlines this process.

An individual scatterometer backscatter measurement $z_i$ can be modeled as the integral of the product of the MRF and the surface backscatter, i.e.,

$$z_i = \iint \text{MRF}_i(x, y; pp)\sigma^o(x, y, \theta, \phi_i, t, pp)dxdy + \text{noise} \tag{1}$$

where $\text{MRF}_i(x, y; pp)$ is the spatial MRF of the i$^{th}$ measurement at $x, y$ and the surface $\sigma^o$ depends on spatial location $x, y$, incidence angle $\theta$, azimuth angle $\phi$, time $t$, and polarization $pp$, i.e.,

$$\text{MRF}_i(x, y; pp) = \iint \frac{G_a^2(x, y; pp)G_p(x, y; pp)}{R^4(x, y)}. \tag{2}$$

where

$$X = \iint \frac{G_a^2(x, y; pp)G_p(x, y; pp)}{R^4(x, y)}dxdy. \tag{3}$$

where $G_a(x, y; pp)$ is the effective two-way antenna gain at the surface at $(x, y)$ for polarization $pp$, $G_p(x, y; pp)$ is the processor gain, and $R(x, y)$ is the slant range from the radar to the surface. Note that the measurement is an average of $\sigma^o$ in spatial coordinates as well as in azimuth and incidence angles.

Eq. 1 is discretized on the imaging grid to become

$$z_i = \sum_{j \in \text{image}} h_{ij}a_j + \text{noise} \tag{4}$$

where $a_j$ is the backscatter at the center of the $j^{th}$ pixel at $(x_l, y_k)$ and $h_{ij} = MRF(x_l, y_k; \phi_i)$ is the discretely sampled MRF for the $i$-th measurement evaluated at the $j$-th pixel center where $h_{ij}$ is normalized so that $\sum_j h_{ij} = 1$. In practice, the MRF is negligible some distance from the measurement center, so the sums need only be computed over a small area around the pixel. Ignoring the noise, Eq. 4 can be written as the matrix equation

$$\vec{Z} = \mathbf{H}\vec{a} \tag{5}$$

where $\mathbf{H}$ contains the sampled MRF for each measurement and $\vec{Z}$ and $\vec{a}$ are vectors composed of the measurements $z_i$ and $a_j$, respectively. Even for small images, $\mathbf{H}$ is large and sparse, and may be over-determined or under-determined depending on the number and locations of the measurements. Reconstruction of the surface $\sigma^o$ is equivalent to inverting Eq. 5.

The iterative SIR algorithm (Early and Long, 2001)(Long et al., 1993) is a particular reconstruction algorithm that is specifically developed for scatterometer image formation.

SIR approximates a maximum-entropy solution to an under-determined equation and a least-squares solution to an over-determined system. The first iteration of SIR is termed 'AVE' (for weighted AVErage) and provides a simple reconstruction estimate that is refined in later SIR iterations. The AVE estimate of the $j$-th pixel is given by

$$a_j = \frac{\sum_i h_{ij} z_i}{\sum_i h_{ij}} \tag{6}$$

where the sums are over all measurements that have non-negligible MRF at the pixel. The SIR iteration begins with an initial image $a_j^0$ whose pixels are set to the AVE values defined in Eq. 6. Thereafter, the iterative equation for single-variate SIR is given by

$$a_j^{k+1} = \frac{\sum_i u_{ij}^k h_{ij}}{\sum_i h_{ij}} \tag{7}$$

where

$$u_{ij}^k = \begin{cases} \left[\frac{1}{2p_i^k}\left(1 - \frac{1}{d_i^k}\right) + \frac{1}{a_j^k d_i^k}\right]^{-1} & d_i^k \geq 1 \\ \frac{1}{2}p_i^k(1 - d_i^k) + a_j^k d_i^k & d_i^k < 1 \end{cases} \tag{8}$$

$$d_i^k = \left(\frac{z_i}{p_i^k}\right)^{\lambda} \tag{9}$$

where $d_i^k = (s_i/p_i^k)^{\lambda}$ with $\lambda = \frac{1}{2}$. The factor $d_i^k$ is the square root of the ratio of a measurement to its forward projection at the $k^{th}$ iteration. The update term $u_{ij}^k$ is a non-linear function of both $d_i^k$ and the previous image $a_j^k$. The sigmoid-like non-linearity in Eq. 8 constrains the amount of change permitted during any one iteration, thereby minimizing the effects of noise Long et al. (1993). Though not used in this paper, a spatial median filter can be applied to the image between iterations to further reduce the noise Long et al. (1993).

For scatterometers, SIR is implemented in dB (Long, 2017)(Early and Long, 2001)(Long et al., 1993); i.e., the computation is done on $10\log_{10}(z_i)$ rather than on the linear-space value $z_i$ as done in the radiometer version of SIR (Long and Brodzik, 2016a)(Long and Daum, 1998). In considering the differences between linear and dB processing, recall the well-known fact that computing the arithmetic mean of values in dB is equivalent to computing $10\log_{10}$ of the geometric mean of the linear-space values (Wikipedia, 2016). With the measurements in dB, the reconstruction processing can be viewed as a form of weighted geometric mean filtering. Since it has been found that geometric mean filters are better at reducing Gaussian-type noise and preserving linear features than (linear) arithmetic mean filters (Pitas and Venetsanopoulos, 1986), some performance advantage to dB processing is expected and observed (Long, 2017). The linear and dB computations yield similar, but slightly different results, due to the varying signal-to-noise ratio (SNR) of the measurements and limited signal dynamic range (Long, 2017).

In practice, since the $\sigma^o$ measurements are quite noisy, attempting full image reconstruction can produce excessive noise enhancement. In general, more iterations improve the signal and resolution, but also increase the noise level. To reduce noise enhancement and resulting artifacts, regularization can be employed, at the expense of resolution (Long and Franz, 2016a)(Early and Long, 2001)(Long et al., 1993)(Long, 2017). Regularization is a smoothing constraint introduced in an inverse problem to prevent extreme values or over-fitting. Regularization results in partial or incomplete reconstruction of the signal (Long and Franz, 2016a). It also creates a trade off between signal reconstruction accuracy and noise enhancement. SIR includes regularization achieved by prematurely terminating the iteration. Based on simulations and confirmed by analysis of actual data, 20-30 iterations provides a nice trade off result. We note that for a noisy sensor like a scatterometer, the results are not particularly sensitive to the precise value chosen, hence a fixed value can be selected. Selection of the number of iterations is based on simulation, see citeearly2001, Long et al. (1993) and Long (2017). For this product, a fixed (30) number of SIR iterations is employed for both binary and full response MRFs.

### 5.3.1 Local-Time-of-Day

As previously noted, the goal of image reconstruction is to estimate the surface $\sigma^o$ from the sensor $\sigma^o$ measurements. Measurements from multiple orbit passes over a narrow local time window are combined. When multiple measurements are combined, the resulting images represent a temporal average of the measurements over the averaging period. There is an implicit assumption that the surface characteristics remain constant over the imaging period For both conventional-resolution (GRD) and enhanced-resolution (SIR) images.

The radar backscatter of a natural surface is a strong function of the state of the water it contains, i.e., frozen or thawed. As a result of the sun-synchronous orbit geometry, the radar observations at a given location on the earth fall within two narrow diurnal windows. At the equator, these correspond to the ascending and descending orbit passes. This can be exploited to provide twice-daily sampling. Thus, *NSCAT* images on the cylindrical *EASE-Grid 2.0* projections are separated by ascending and descending passes. A separate image ("both") product is also made that combines both which achieves between spatial coverage at the expense of temporal resolution.

Near the poles, the temporal windows widen to several hours but remain relatively narrow. Since surface temperatures can fluctuate widely during the day, daily averaging is not generally useful at these locations, since it smears diurnal temperature fluctuations in the averaged $\sigma^o$. However, it is reasonable to split the data into two distinct images per day, using intervals based on local-time-of-day (ltod), thereby only combining measurements with a similar ltod. This minimizes the fluctuations in the observed backscatt at high latitudes due to changes in physical temperature from daily temperature cycling.

The *NSCAT* images on the azimuthal projections are separated into twice-daily, morning

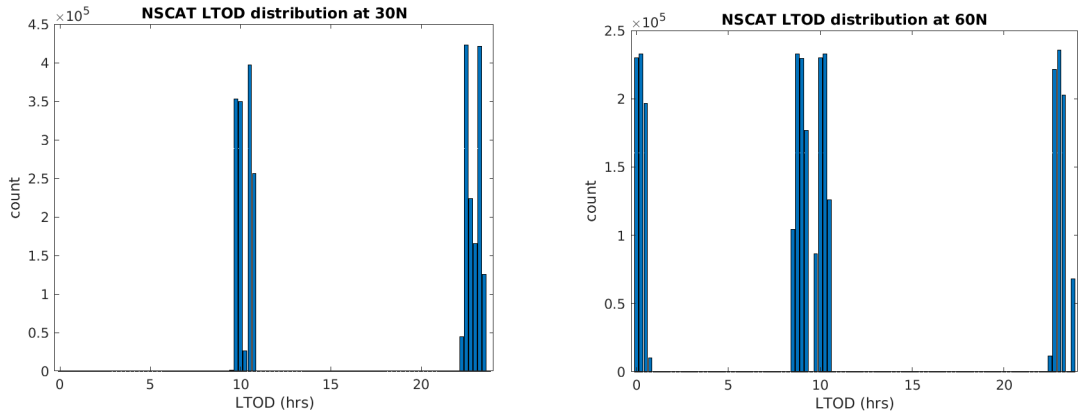


**Figure 14:** *Histograms of typical measurement ltod for NSCAT measurements falling within a* $1°$ *latitude band at (left)* $30°$–$31°$ *N and (right)* $60°$–$61°$ *N over one day. All measurements fall into essentially one of two narrow ltod time periods, centered at approximately 00:00 h and 10:00 h in the Northern Hemisphere. Although the center time varies with latitude, any point on Earth is observed at one of two times within* $\pm 90\,\mathrm{min}$.

and evening passes based on observation ltod, in addition to images that combine the two. At low latitudes, which typically have few overlapping swaths at similar ltod in the same day, ltod division is equivalent to ascending/descending division. An ancillary data array is included in each file, to describe the effective time average of the measurements combined into the pixel for a particular day. This enables investigators to explicitly account for the ltod temporal variation of the measurements included in a particular pixel. A separate image ("both") product is also made that combines both which achieves greater spatial coverage at the expense of temporal resolution.

Histograms of the ltod of the sensor's measurements falling within two narrow latitude bands are shown in Fig. 14. For the NSCAT orbit, a natural division in the measurement ltod is at 00:00 and 12:00 h. For consistency with Long and Brodzik (2016b) and Brodzik et al. (2021), the *NSCAT* data are produced using this ltod division. Note how the ltod falls within one of two tight groups that correspond to the ascending and descending orbit passes, and that there are natural divisions in the measurement ltod at 00:00 and 12:00 hrs. Thus, the measurements provide twice-daily sampling. Note that when more than day's worth of data, the ltod division is maintained so that a multi-day morning image combines only morning observations.

## 5.4 Sample Data

Figures 15–17 present examples of 8-day product images for each polarization and region where all passes ('both') within the imaging period are combined. Swath-like artifacts

over the oceans are the result of significant temporal variation of surface $\sigma^o$ due to wind changes during the imaging interval. Over the ocean high winds correspond to higher $\sigma^o$ values while low winds correspond to low wind speeds. Additional data visualization are provided in later sections.

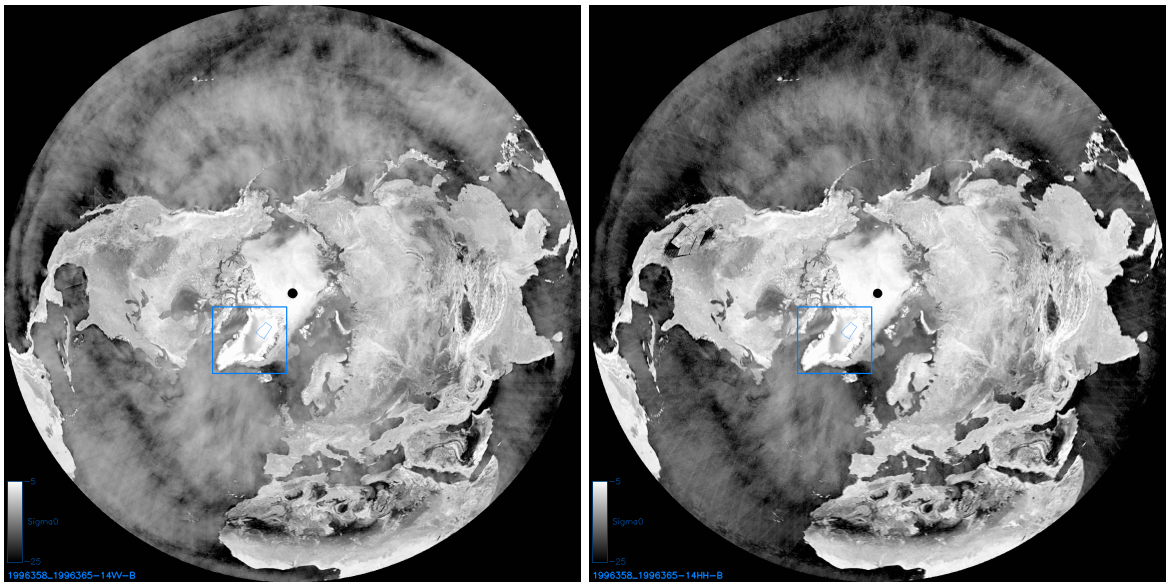


**Figure 15:** *Visualizations of examples of 8-day (DOY 351-358, 1996) NSCAT A ($\sigma^o$ at 40° incidence angle) for (left) VV and (right) HH polarizations. Images have been reduced in resolution for presentation here. The large Greenland study area is outlined. See captions for Figs. 17 and 18.*

**Table 6:** *Study Sub Regions*

| Region | Longitude | | Latitude | | $A_{HH}$ | $B_{HH}$ | $A_{VV}$ | $B_{VV}$ |
|---|---|---|---|---|---|---|---|---|
| | left | right | lower | upper | dB | dB/deg | dB | dB/deg |
| Amazon | 294 | 295.5 | -6 | -4 | -7.12 | -0.0684 | -7.47 | -0.0836 |
| Congo | 19 | 21.5 | -1.5 | 1.25 | -6.63 | -0.0486 | -7.08 | -0.0677 |
| Greenland (large) | 317 | 328 | 75 | 79 | -5.17 | -0.1813 | -4.32 | -0.1347 |
| Greenland* (small) | 312 | 328 | 70 | 70.25 | – | – | – | – |
| Pampas | 299 | 300 | -37 | -35 | -10.82 | -0.1468 | -11.53 | -0.1359 |

*Each small Greenland subregion spaced 2 deg of longitude has longitude extent 0.5 deg

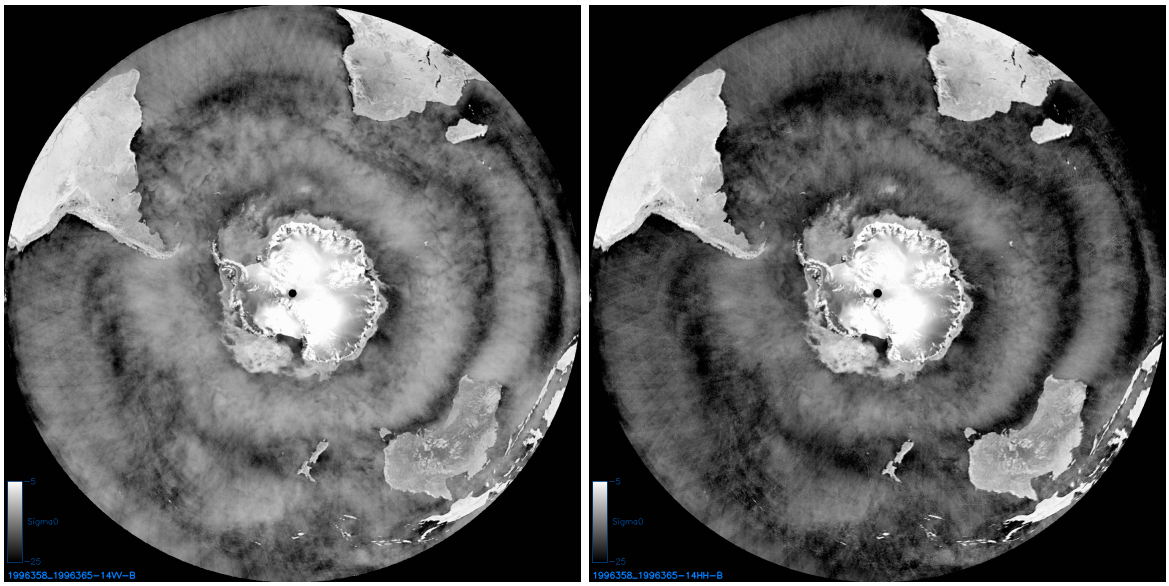


**Figure 16:** *Visualizations of examples of 8-day (DOY 351-358, 1996) NSCAT A ($\sigma^o$ at 40° incidence angle) for (left) VV and (right) HH polarizations. Images have been reduced in resolution for presentation here.*

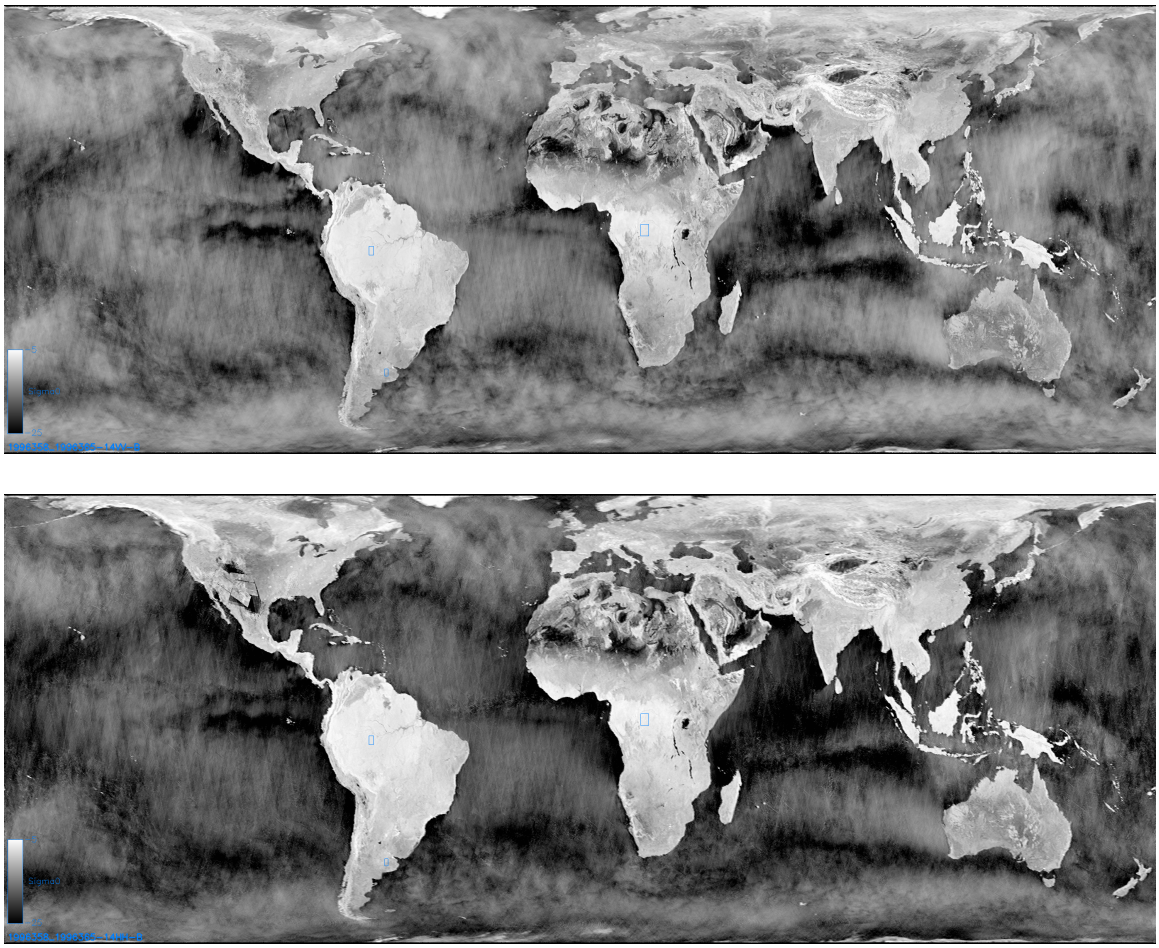

**Figure 17:** *Visualizations of examples of 8-day (DOY 351-358, 1996) NSCAT A ($\sigma^o$ at 40° incidence angle) for (top) VV and (bottom) HH polarizations. Images have been reduced in resolution for presentation here. Blue boxes show study regions used later. The image artifacts in Western North America are from missing data resulting from instrument mode variations to support a ground calibration ground station in New Mexico.*

# 6 Measurement Modeling

To dive deeper into the backscatter data and the performance of the imaging algorithms, we define a number of study regions in Greenland, see Fig. 18 and Tab. 6. The coastal region is employed to visualize the differences between the products at fine resolution in Figs. 19–24.

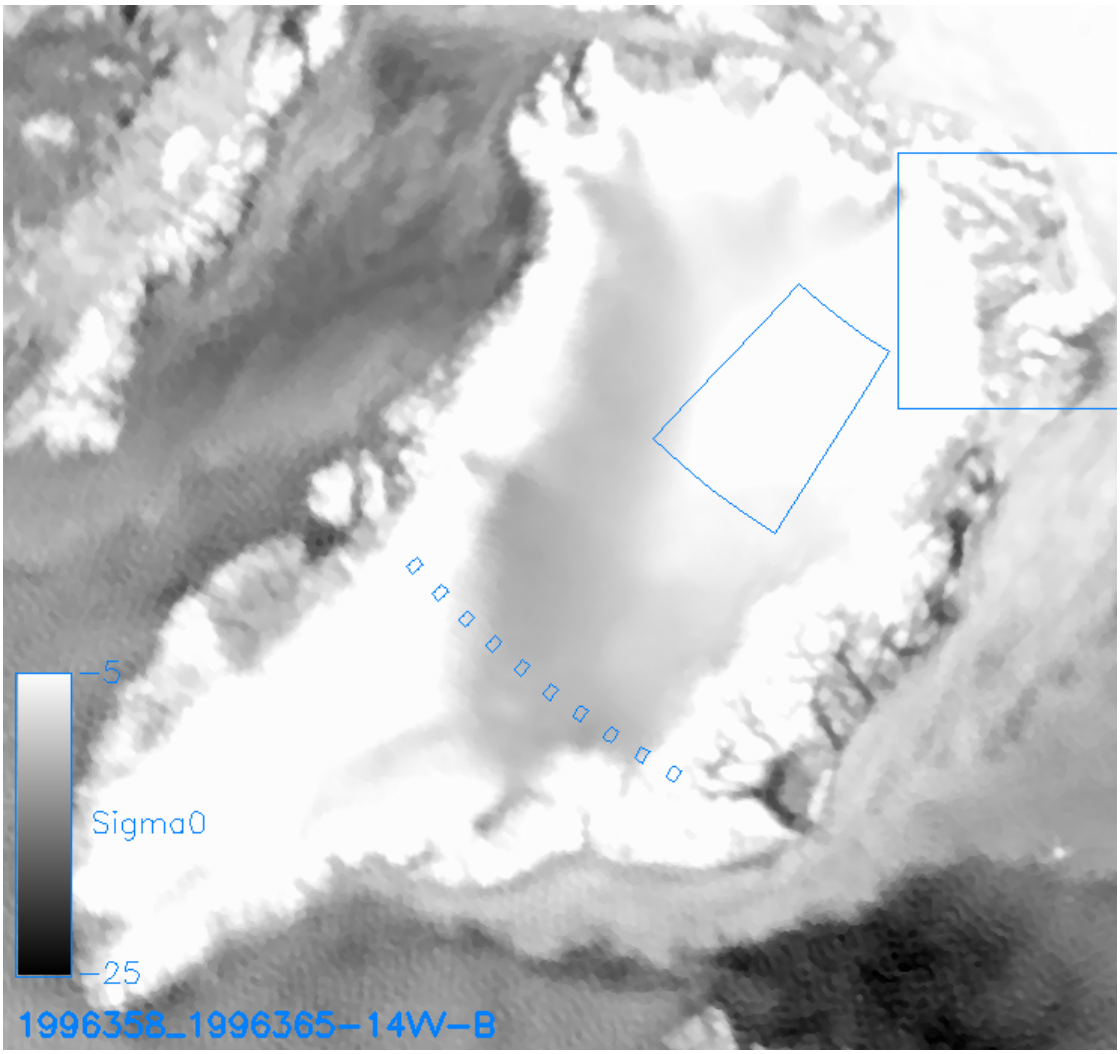


**Figure 18:** *Sample 8 day both pass VV pol A image of the Greenland study area outlined in Fig. 15. Subregions considered in later figures are outlined, see Tab. 6.*

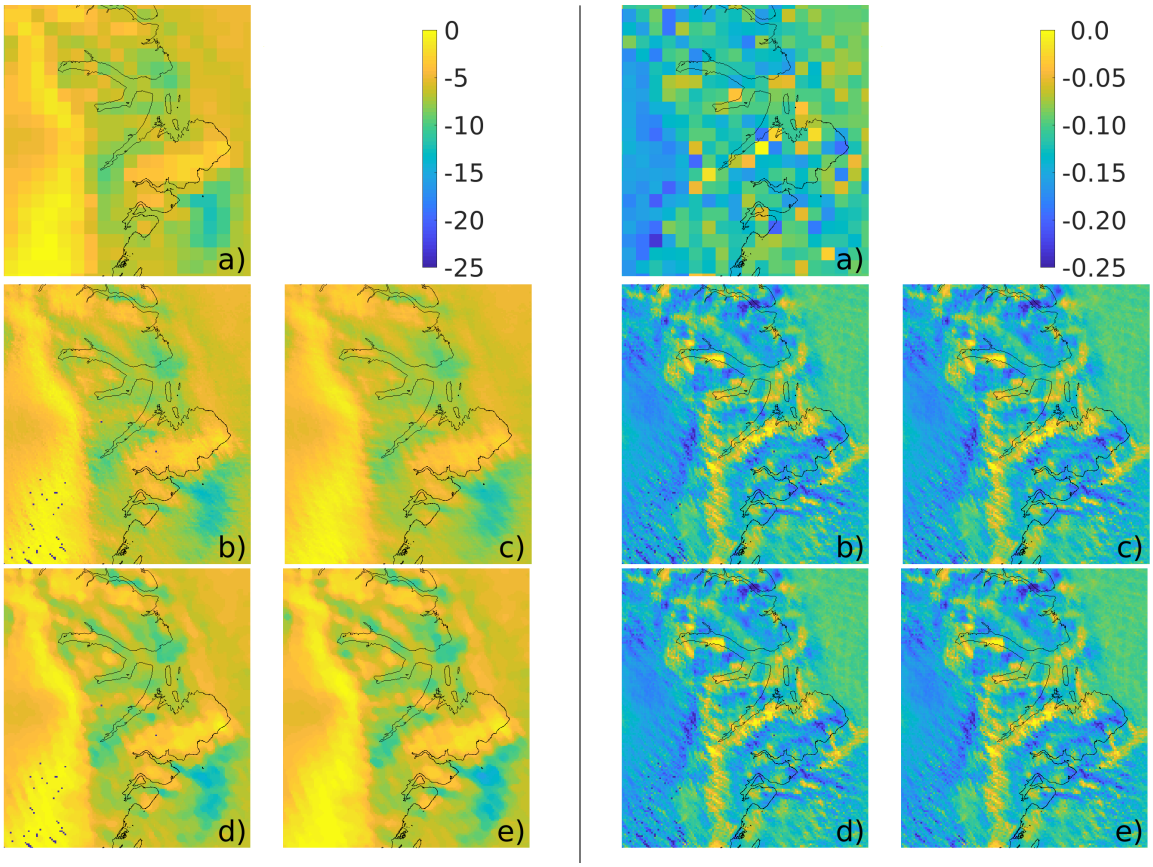


**Figure 19:** *Comparison of HH polarization all-pass 8 day images for DOY 346-353, 1996. (left side) A in dB. (right side) B in dB/deg. (a) 25 km pixel GRD image. (b) 3.125 km pixel binary response AVE. (c) 3.125 km pixel full response AVE. (d) 3.125 km pixel binary response SIR. (e) 3.125 km pixel full response SIR. Black spots in the binary response images are pixels not included in the binary response coverage. Texture artifacts result from limited measurement overlap and coverage during the imaging interval, which are more severe for H-pol.*

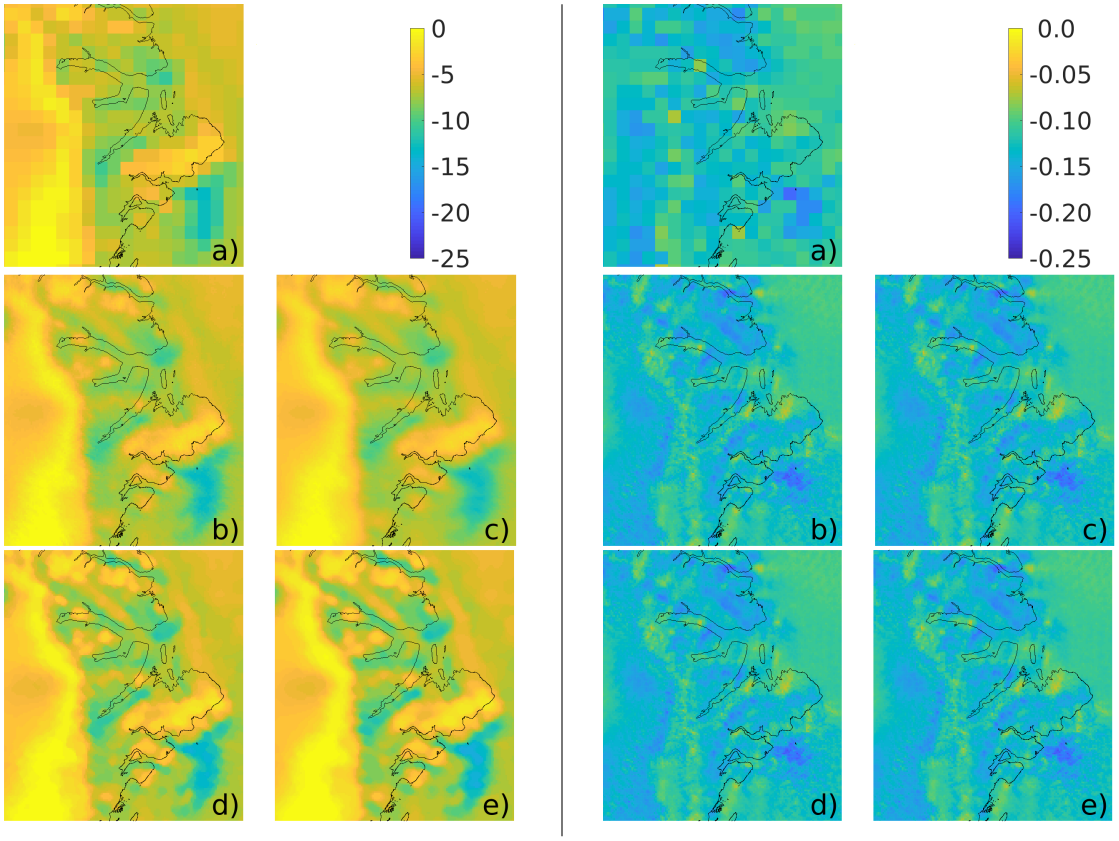


**Figure 20:** *Comparison of VV polarization all-pass 8 day images for DOY 346-353, 1996. (left side) A in dB. (right side) B in dB/deg. (a) 25 km pixel GRD image. (b) 3.125 km pixel binary response AVE. (c) 3.125 km pixel full response AVE. (d) 3.125 km pixel binary response SIR. (e) 3.125 km pixel full response SIR. Black spots in the binary response images are pixels not included in the binary response coverage. Texture artifacts result from limited measurement overlap and coverage during the imaging interval.*

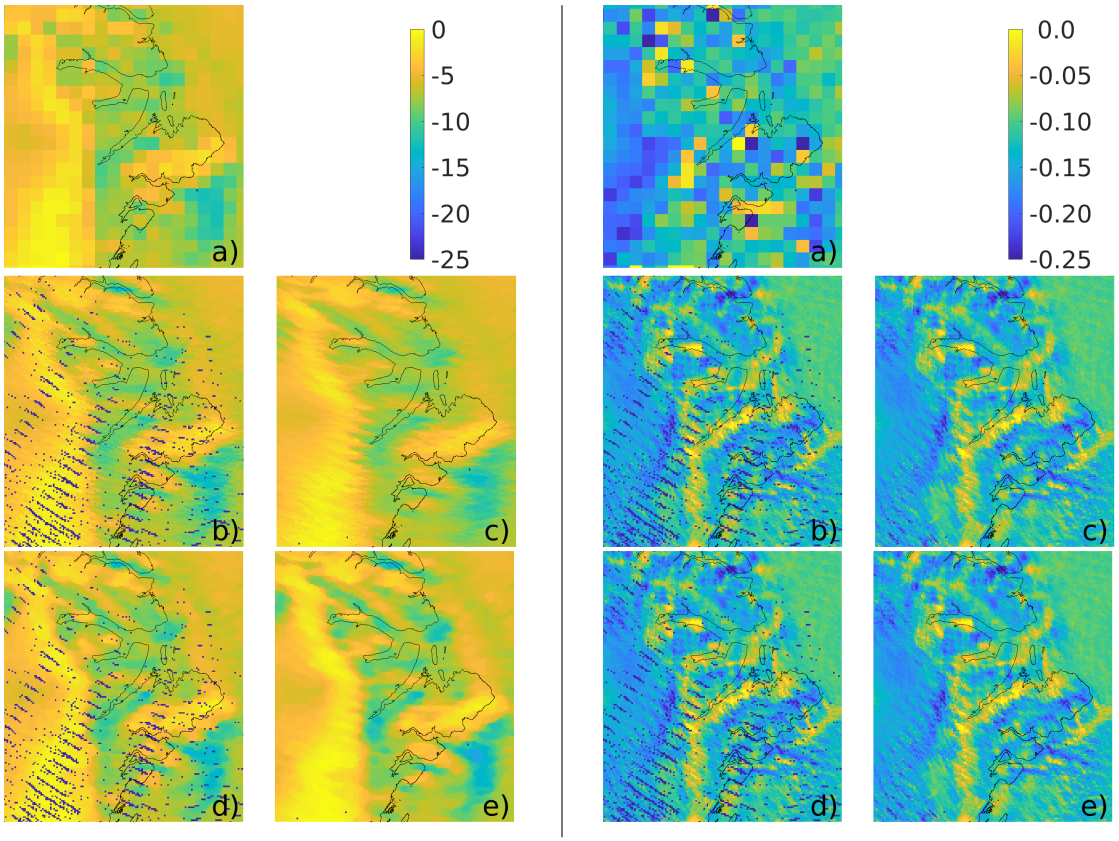


**Figure 21:** *Comparison of HH polarization evening-pass 8 day images for DOY 346-353, 1996. (left side) A in dB. (right side) B in dB/deg. (a) 25 km pixel GRD image. (b) 3.125 km pixel binary response AVE. (c) 3.125 km pixel full response AVE. (d) 3.125 km pixel binary response SIR. (e) 3.125 km pixel full response SIR. Black spots in the binary response images are pixels not included in the binary response coverage. Texture artifacts result from limited measurement overlap and coverage during the imaging interval, which are more severe for H-pol.*

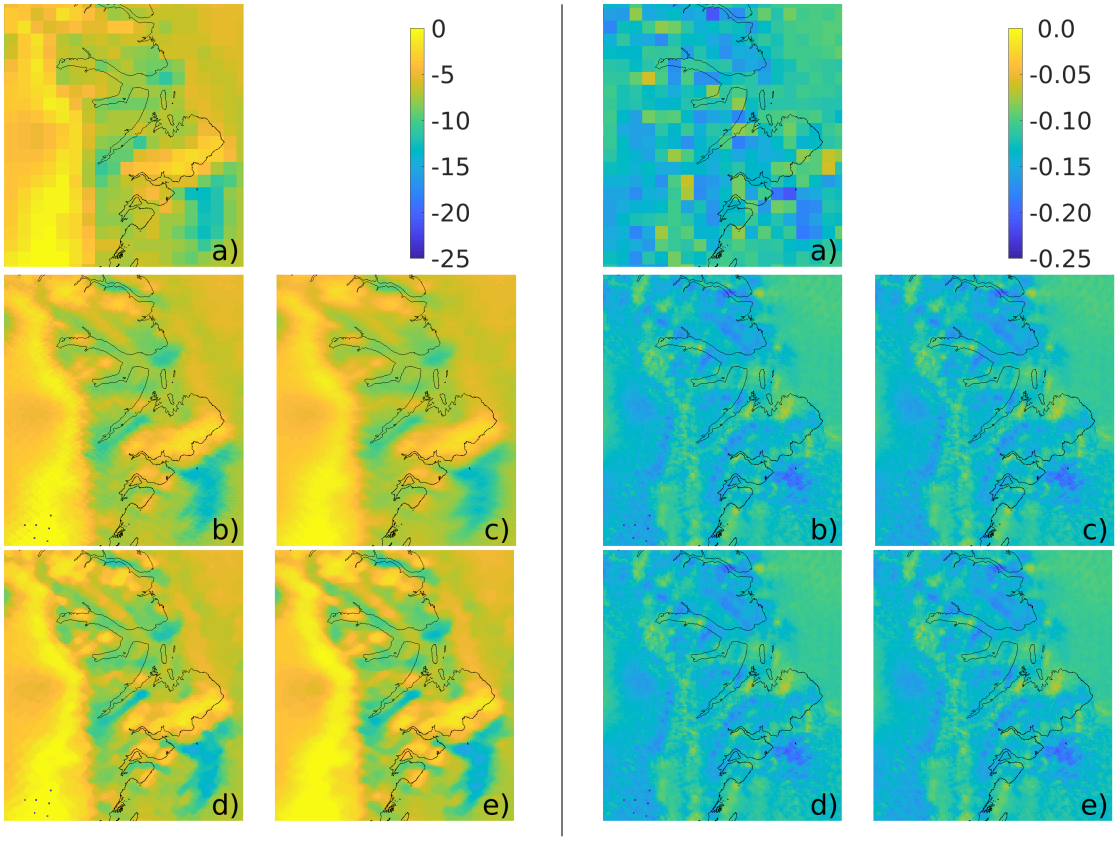


**Figure 22:** *Comparison of VV polarization evending-pass 8 day images for DOY 346-353, 1996. (left side) A in dB. (right side) B in dB/deg. (a) 25 km pixel GRD image. (b) 3.125 km pixel binary response AVE. (c) 3.125 km pixel full response AVE. (d) 3.125 km pixel binary response SIR. (e) 3.125 km pixel full response SIR. Black spots in the binary response images are pixels not included in the binary response coverage. Texture artifacts result from limited measurement overlap and coverage during the imaging interval.*

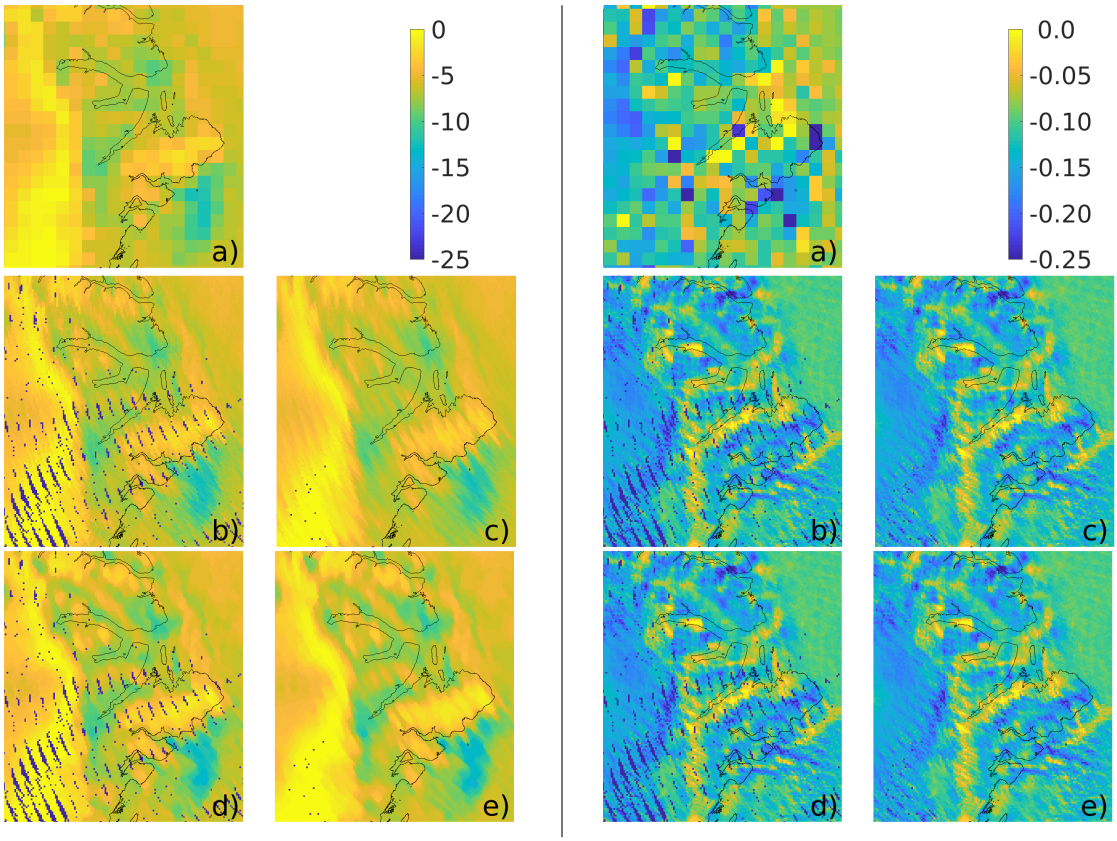


**Figure 23:** *Comparison of HH polarization morning-pass 8 day images for DOY 346-353, 1996. (left side) A in dB. (right side) B in dB/deg. (a) 25 km pixel GRD image. (b) 3.125 km pixel binary response AVE. (c) 3.125 km pixel full response AVE. (d) 3.125 km pixel binary response SIR. (e) 3.125 km pixel full response SIR. Black spots in the binary response images are pixels not included in the binary response coverage. Texture artifacts result from limited measurement overlap and coverage during the imaging interval, which are more severe for H-pol.*

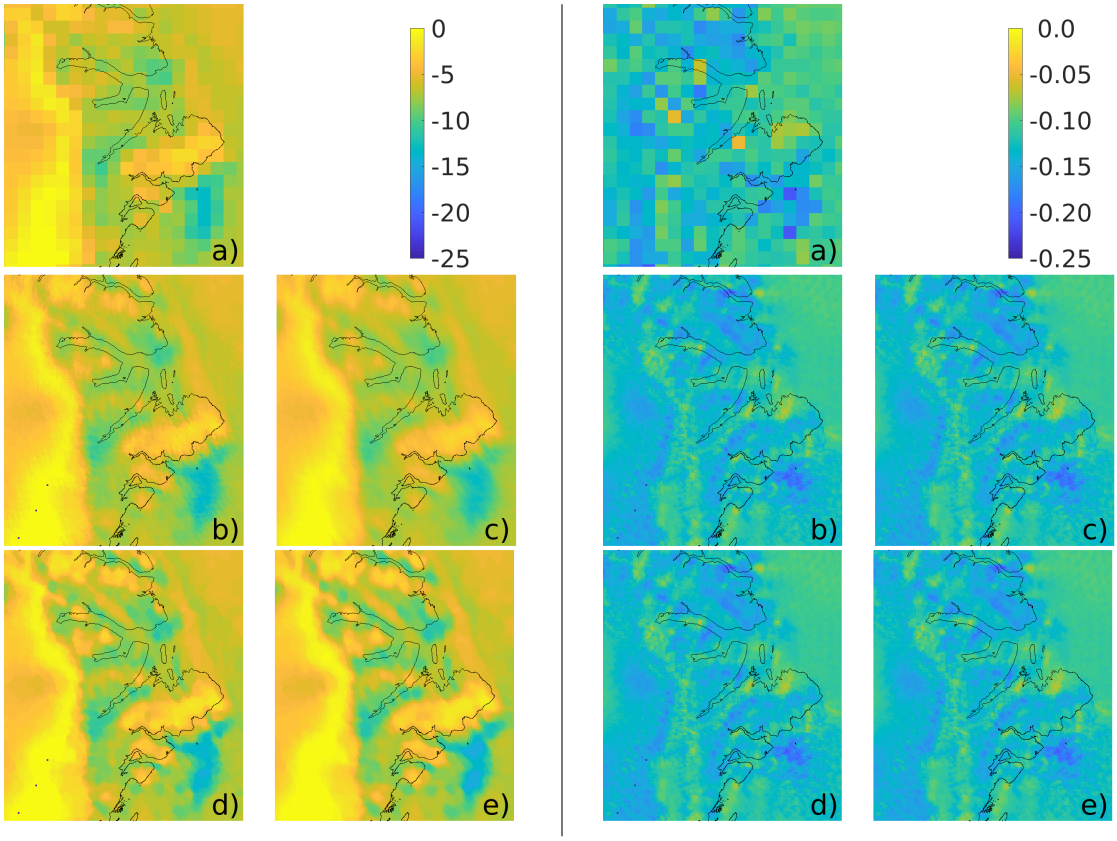


**Figure 24:** *Comparison of VV polarization morning-pass 8 day images for DOY 346-353, 1996. (left side) A in dB. (right side) B in dB/deg. (a) 25 km pixel GRD image. (b) 3.125 km pixel binary response AVE. (c) 3.125 km pixel full response AVE. (d) 3.125 km pixel binary response SIR. (e) 3.125 km pixel full response SIR. Black spots in the binary response images are pixels not included in the binary response coverage. Texture artifacts result from limited measurement overlap and coverage during the imaging interval.*

## 6.1 Incidence Angle Effects

Over natural surfaces $\sigma^o$ depends on the measurement incidence angle. Since NSCAT is a fan-beam system, it collects $\sigma^o$ measurements over a range of incidence angles ranging from about 15° to 60°. The variation in incidence angle must be accounted for when combining multiple measurements. The incidence angle normalization $\gamma^o = \sigma^o / \cos\theta$ where $\theta$ is the incidence angle is sometimes used. However, the slope of this correction is strictly downward and since upward slopes are observed in some areas, this normalization is not used. Instead, following prior investigators, see Long et al. (1993) and references therein, a linear slope is used that is centered at 40°, i.e., $\sigma^o$ as a function of incidence angle is modelled according to

$$\sigma^o = A + B(\theta - 40^\circ) \tag{10}$$

where $A$ is $\sigma^o$ at 40° incidence angle; $B$ is the slope of $\sigma^o$ versus incidence angle $\theta$. At each pixel, the model parameters $A$ (the mean $\sigma^o$), $B$ (the normalized slope of $\sigma^o$ versus incidence angle are estimated from the backscatter measurements on a pixel by pixel basis.

Note that there is a variation (typically $<1^\circ$) in incidence angle over the the footprint of each measurement. Because the measurements integrate the echo return over the measurement MRF, only a single $\sigma^o$, mean incidence angle, and mean azimuth angle value is reported for an NSCAT measurement. The measurements essentially average the incidence and azimuth angle dependence over the MRF. While the *intra*-measurement angle variation is small, the *inter*-measurement the variation in incidence angle between measurements is much larger, and has a significant effect.

To explore this, some small (0.5° longitude by 0.25° latitude) study regions are defined in the Greenland Ice Sheet, see Fig. 18. The regions are individually small enough to have nearly spatially constant scattering characteristics, but span the range of ice facies Long and Drinkwater (1994) over the ice sheet with a variety of mean $\sigma^o$ values. Figures 25 and 26 shows the variation in incidence angle for measurements collected over each of these study regions during a 41-day interval. Noting the sloping dependence of $\sigma^o$ (and $\gamma$ with incidence angle. Linear least-squares (in both linear space and with $\sigma^o$ in dB) fits of $\sigma^o$ versus incidence angle are shown as solid lines. The coefficients of the the linear ($\sigma^o$ in dB) fit are included in Tab. 6. In Fig. 26 scaled coefficients of the fits (in dB) are included as overprinted values. In each panel, the top line is linear fit with $A$ (the mean value at 40 deg incidence angle) on the left and $B$ (the slope) times 10 on the right. The second line shows the coefficients of the quadratic fit with $A$ on the left, $B$ times 10 in the center and $C$ times 1000. The third line is the coefficients of the cubic fit with $A$ on the left, $B$ times 10 left of center, $C$ times 1000 right of center and $D$ times 10000 on the right where

$$\sigma^o = A + B(\theta - 40) + B(\theta - 40)^2 + C\theta - 40)^3. \tag{11}$$

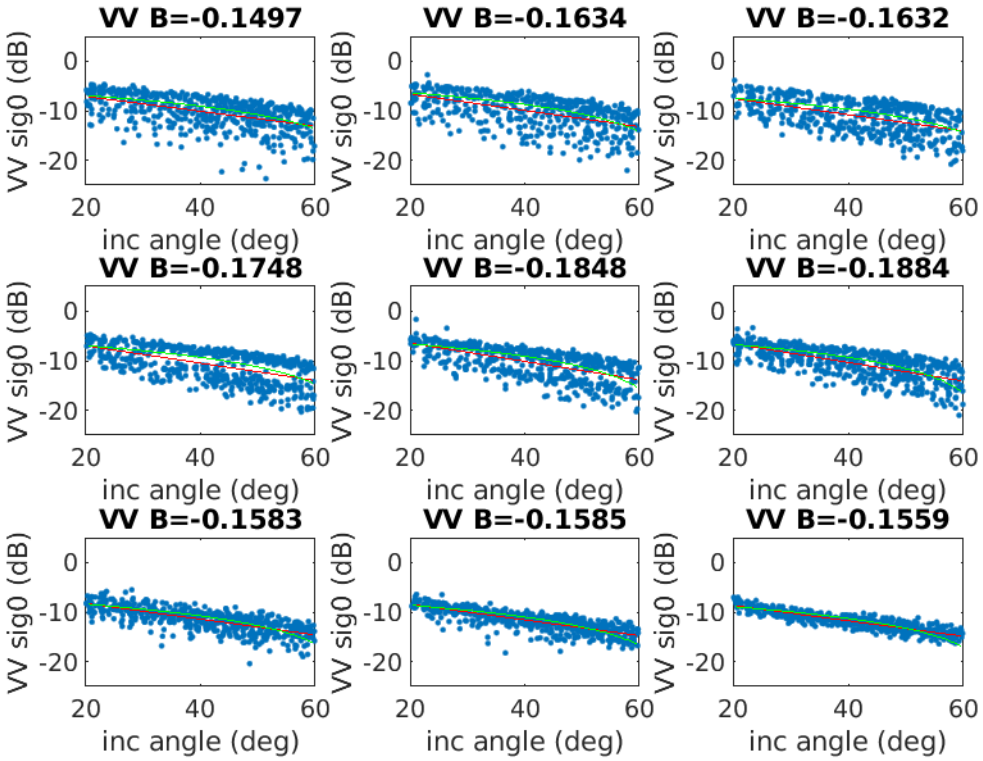


**Figure 25:** *Vertically-polarized $\sigma^o$ versus incidence angle for Greenland sub regions showing (red) $\sigma^o$ in dB linear fit and (green) $\sigma^o$ and (green) $\sigma^o$ in normal space (not dB) linear fit to the data. Panel titles give the slope $B$ in dB/deg for the $\sigma^o$ in dB model. Because of the small sub region size, a long time interval spanning two orbit repeat cycles (82 days) from DOY 271 to DOY 353 was used. Refreezing of firn in areas some regions result in two different populations of data over long time interval.*

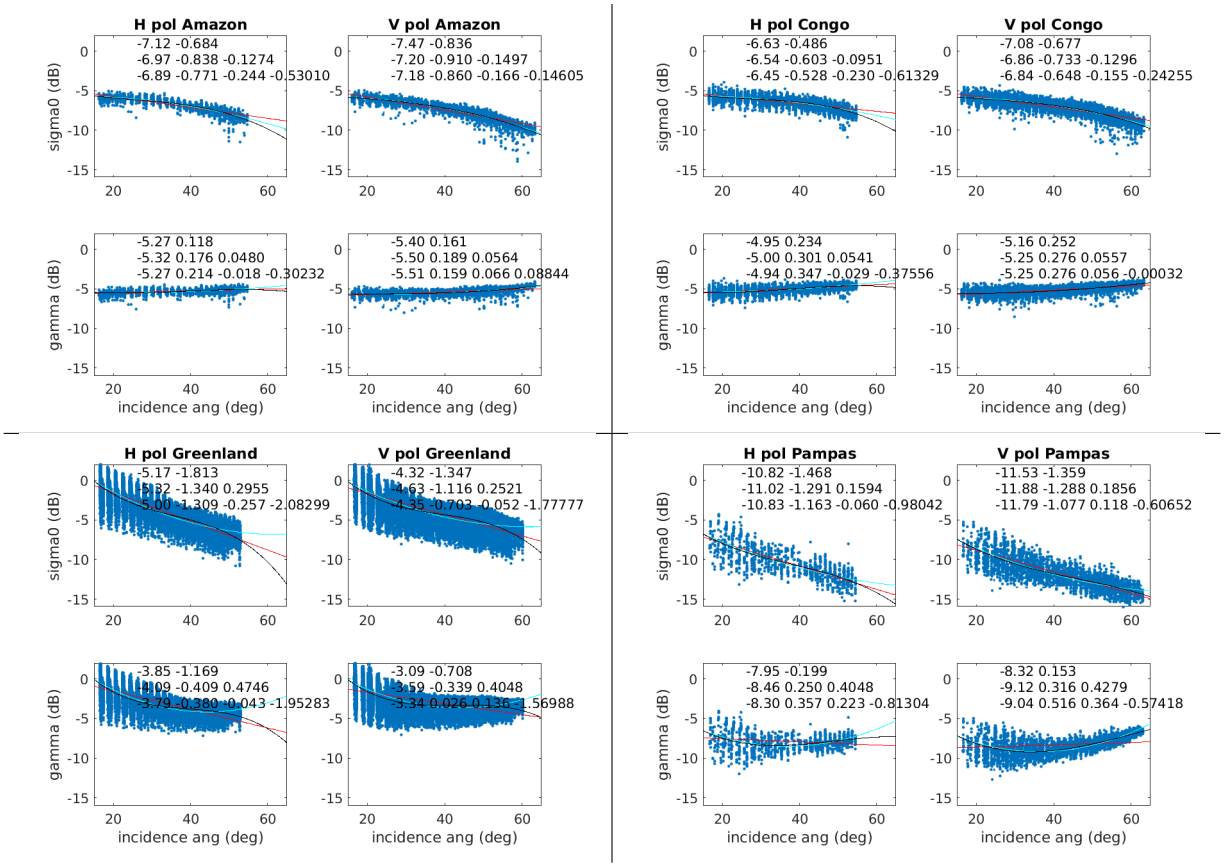


**Figure 26:** *$\sigma^o$ and $\gamma$ versus incidence angle for four study regions of varying locations and size with different surface types showing (red) linear, (green) quadratic, and (black) cubic $\sigma^o$ in dB versus incidence angle fits to the data. Data is from DOY 271–353, 1997 all passes. See text regarding numbers on plot.*

## 6.2 Azimuth Angle Effects

Periodic natural surfaces exhibit variations in $\sigma^o$ with azimuth angle, including water waves Ulaby and Long (2014), Naderi et al. (1991), sastrugi[2] and snow dunes (Long and Drinkwater, 2000)(Lindsley and Long, 2016)(Ashcraft and Long, 2006), and sand dunes Stephen and Long (2007). The measured $\sigma^o$ is thus a function of the azimuth direction from which the surface is observed. Scatterometers such as NSCAT are *designed* to make multi-azimuth observations over the ocean to exploit this effect for wind-driven wave in order to estimate the near-surface wind Naderi et al. (1991). However, these measurements intrinsically coarse since they must be made in a single pass. Unlike the ocean, land and ice features do not (generally) change as rapidly so observations from multiple passes can be combined.

Over the course of the orbit's repeat cycle each point on the surface can be observed at multiple azimuth angles. For example, as the spacecraft passes over a particular location within the swath, the location is first observed looking, then a short while later the same location is observed looking backward. Over the orbit repeat cycle, the ground track shifts so that the same location is observed from a different set of azimuth angles for each pass. The precise distribution of azimuth angles depends on the orbit latitude, with the narrowest range near the equator and the largest range at high latitudes.

Note that there is a trade off between the imaging time period, the spatial resolution, and the azimuth sampling. Short time periods provide better temporal resolution for tracking sea ice motion and rapid freeze thaw events. However, short time periods provide inadequate coverage and/or azimuth sampling to reliably estimate the azimuth angle variation, particularly when the data is divided by local time of day. Recalling that the orbit repeat cycle is near-repeat after 4 days, we choose $N_d$ =4 and $N_d$ =8 day imaging intervals ($N_d$ in days[3]. The imaging intervals are chosen to overlap by $N_d - 1$ days so they act like a $N_d$ long moving average filter. Shorter $N_d$ provides finer temporal resolution at the expense of reduced spatial coverage/resolution, including possible spatial artifacts in the reconstruction. These negative effects are reduced for the longer imaging intervals.

Note that a particular $\sigma^o$ observation is an average of $\sigma^o$ in spatial coordinates as well as in azimuth and incidence angles. Within a single measurement the azimuth angle span ($<1^\circ$) for a particular measurement is small and can be neglected. The incidence angle span within a single measurement can be slightly larger ( 1-1.5$^\circ$). The roll off of $\sigma^o$ versus incidence angle, slightly biases the integrated measurement toward smaller incidence angles. This effect is neglected.

On the other hand, the variation in $\sigma^o$ as a function of azimuth and incidence angles for different measurements is important and provides useful geophysical information. Incidence angle variation is considered in the previous section. Of source, the variation in

[2]Sastrugi are wave-like features created by wind erosion and deposition of snow.

[3]Imaging intervals are specified in days, but may include only morning or evening (or descending or ascending) passes depending on the ltod setting.

$\sigma^o$ as a function of azimuth is enables wind retrieval over the ocean (Ulaby and Long, 2014)(Meissner et al., 2017). Azimuth variation (sometimes termed 'azimuth modulation') can be observed over snow dunes and sastrugi (Long and Drinkwater, 2000)(Ashcraft and Long, 2006)(Lindsley and Long, 2016) and sand dunes in ergs[4] (Stephen and Long, 2007). As a result, significant azimuth variation in $\sigma^o$ is common over the Great Ice Sheets (GI) of Greenland and Antarctica, but is only rarely observed elsewhere over large regions with the exceptions of ergs.

For fan-beam scatterometers, since each satellite pass observes a given point on the surface from a limited azimuth angle, the variation of $\sigma^o$ with azimuth can lead to biases in the mean $\sigma^o$ value and to imaging artifacts when multiple passes with different azimuth angle observations are combined. To deal with azimuth variation of $\sigma^o$ on the GI, previous investigators, e.g., Long and Drinkwater (2000), Ashcraft and Long (2006), and Lindsley and Long (2016), have used a simple Fourier series model for the azimuth variation observed in $\sigma^o$. Two models have been considered. One (here termed 'FA') with fixed azimuth modulation coefficients and the other (here termed 'VA') with incidence angle-dependent azimuth modulation coefficients. The azimuth modulation models can be expressed as

$$\sigma^0 = A + B(\theta - 40) + M_1 \cos(\phi + P_1) + M_2 \cos(2\phi + P_2) \tag{12}$$

where $\phi$ is the azimuth angle, $M_1 = A_1$ and $M_2 = A_2$ for the FA model, and $M_1 = A_1 + R_1(\theta - 40)$ and $M_2 = A_2 + R_2(\theta - 40)$ for the VA model where $A_1$ and $A_2$ are the mean azimuth modulation coefficients and $P_1$ and $P_2$ are the phase angles relative to north. Note that the model can be with $\sigma^o$ in dB or linear space, though dB model have proven to the the most successful (Long and Drinkwater, 2000)(Lindsley and Long, 2016).

Following their work, we use a similar approach for modeling the azimuth variation of $\sigma^o$ for the azimuth image products described below. This technique, while applied globally, is most useful over the GI in the polar regions. Over over other land areas, the amplitude of azimuth angle variation is small (though occasionally becomes visible as swath-related artifacts or in small image-to-image "oscillations" in $A$ due to variations in the distributions of the incidence and azimuth angles of observations).

Unfortunately, with a maximum of only 2 azimuth angles in a single pass, the NSCAT HH polarization geometry is not very well suited for estimating the azimuth variation. The maximum of 6 azimuth angles for VV polarization is only somewhat better. Complicating matters further is that in the polar regions the incidence angle and azimuth angle of the observations at a given point may be coupled for the fan-beam geometry (Long and Drinkwater, 2000), see Fig. 28. Due to computational limitations, azimuth images are only available with AVE reconstruction. For SIR products azimuth dependence is ignored. HH polarization azimuth images are only created with 16 day imaging intervals.

Figures 29 and 29 illustrate various AVE azimuth product images. Note that the estimation of the azimuth model coefficients assumes a stationary surface. Because of the

[4]An erg landform is a large region or 'sea' of vegetation-free, wind-swept desert sand.

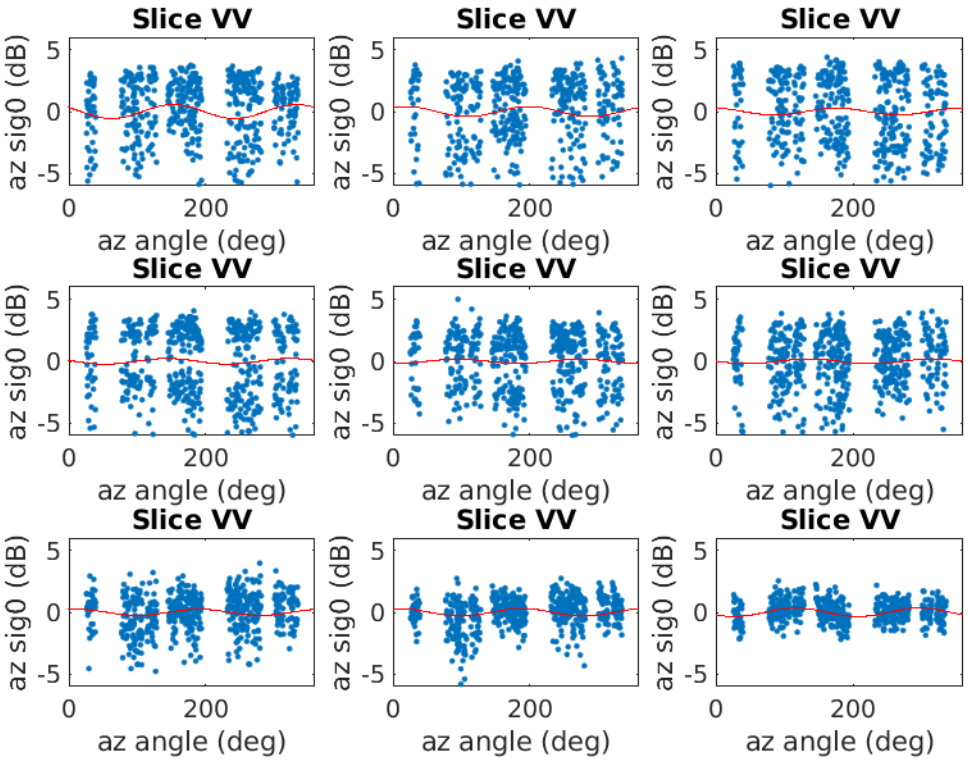


**Figure 27:** *$\sigma^o$ versus azimuth angle relative to north for Greenland subregions with 1st order azimuth modulation fit shown in red. Individual $\sigma^o$ measurements have been corrected for incidence angle and adjusted to zero mean. The individual plots are for the sub regions within the larger Greenland study area.*

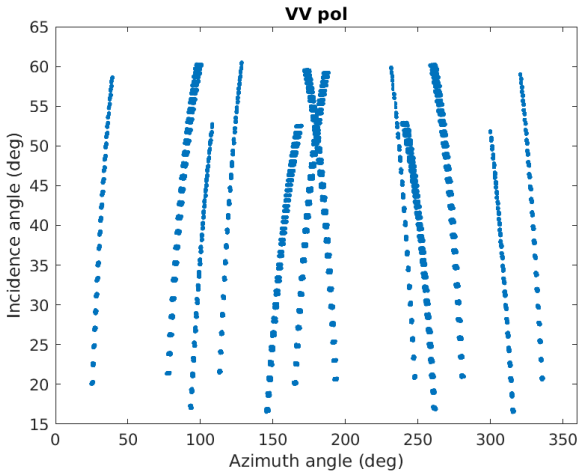


**Figure 28:** *VV polarization azimuth angle relative to north versus incidence angle for the Greenland study region.*

wind variability over the ocean during the imaging period, the estimated azimuth model parameters should not be used.

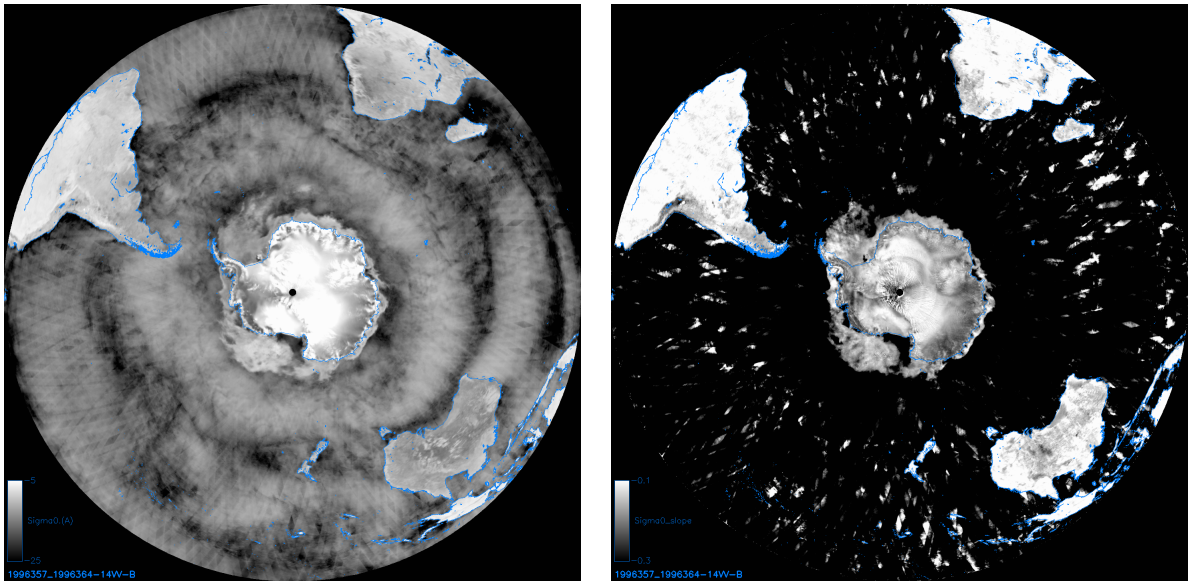


**Figure 29:** *Southern Hemisphere VV (left) $\sigma^o$ (A) and (right) $\sigma^o$ slope (B) images for DOY 357-364, 1996. Image resolution has been reduced for display here.*

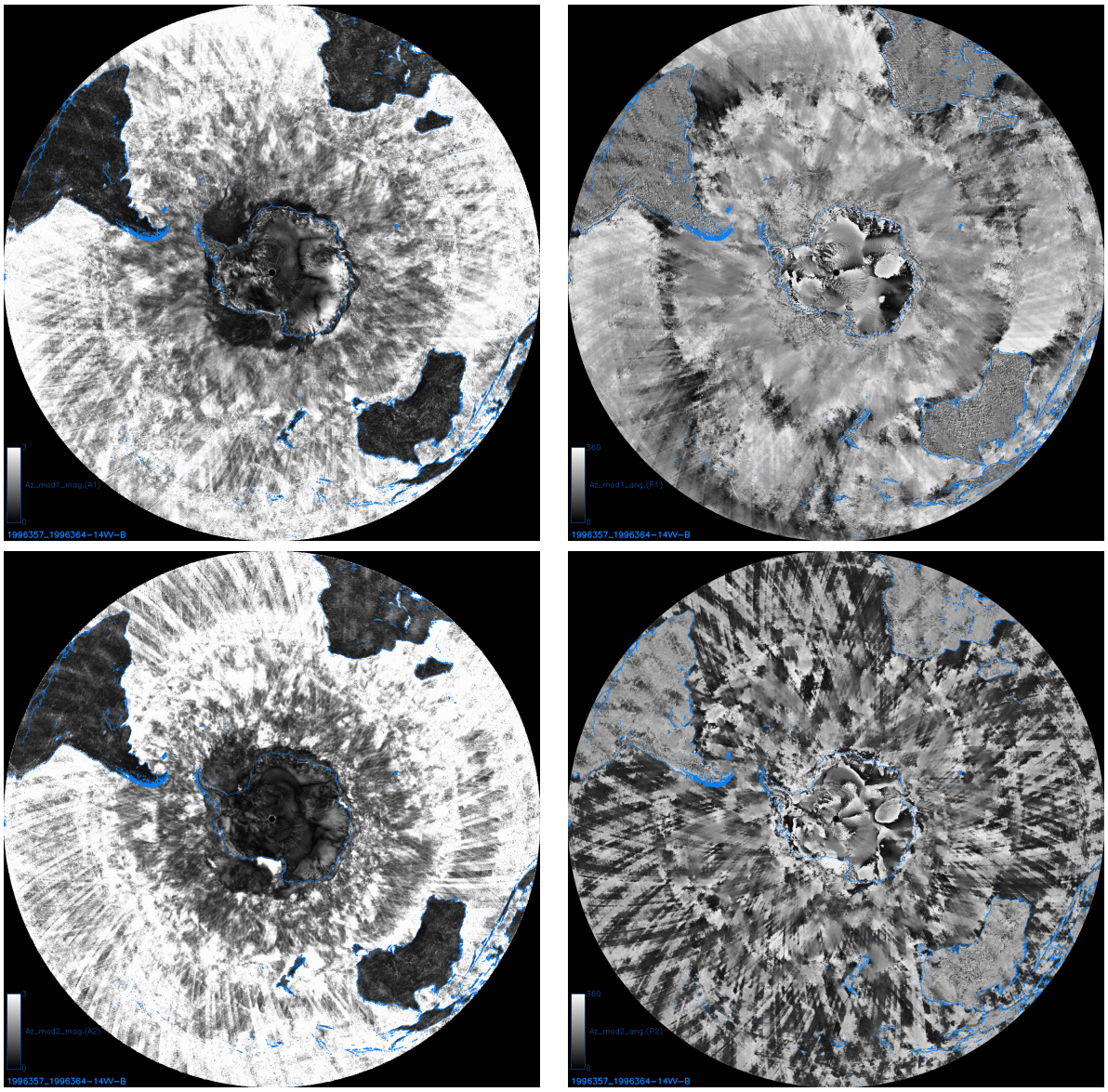

**Figure 30:** *Southern Hemisphere VV $\sigma^o$ azimuth model coefficient images for DOY 357-364, 1996. (upper-left) $A_1$ magnitude. (upper-right) $P_1$ angle. (lower-left) $A_2$ magnitude. (lower-right) $P_2$ angle. Image resolution has been reduced for display here.*

## 6.3 Binary Versus Full Response Images

In creating the CETB *NSCAT* radar product, separate image products were generated using the binary approximation and the full MRF. There are advantages to both approaches, so the user must select which is the most appropriate for their study. This section is provided to further understand the trade offs between the two MRF options. See Section 4.2 for the details on the two MRF options.

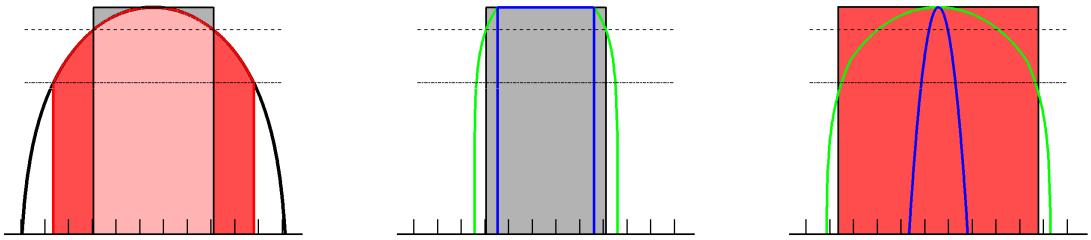

**Figure 31:** *Notional plots of binary and full response MRFs and corresponding PSRFs for one and multiple measurements using AVE. In these one-dimensional illustrations only the main lobe of the MRF is shown. (left) The solid black line shows the true normalized MRF in dB versus distance. The gray box is the binary (1/0) rect-function approximation. The red line is the full response MRF used, which is the full response MRF that is truncated to some threshold value (-10 dB in this example). (center) Effective PSRF estimate when the binary approximation is used. The gray box is the result when only a single measurement is available. The green line corresponds to the PSRF estimate when a dense set of measurements are available and the image formation is done in linear (not dB) space. The blue line corresponds to the PSRF estimate when a dense set of measurements are available and the image formation is done in dB space. (right) Effective PSRF estimate when the truncated full MRF is used. The red box is the result when only a single measurement is available. The green line corresponds to the PSRF estimate when a dense set of measurements are available and the image formation is done in linear (not dB) space. The blue line corresponds to the PSRF estimate when a dense set of measurements are available and the image formation is done in dB space. In all the plots, the upper dashed line is the half-power (-3dB) level below the peak value at 0 dB. The dash-dot line is the -10 dB level. The small lines illustrate the spacing of the fine resolution pixels in which the final image is reported in.*

As described in Section 5.1, the PSRF is defined by the weighted combination of the MRFs of the measurements included in the pixel value. The weighting is determined by the choice of the algorithm used to create the image. This can be illustrated with the notional plots in Fig. 31 for AVE.

Unfortunately, the NSCAT measurement sampling does not fully cover the surface in a single pass, i.e., the surface is undersampled, so there are areas of pixels with only a single measurement available. For this case, the AVE (and therefore the SIR) image can only report

this measurements' value over the area of its non-zero MRF and no resolution enhancement occurs. In fact, depending on the choice of the MRF used in the imaging process (i.e., binary or full response), the reported image has a different effective resolution. As illustrated in Fig. 31, when only a single measurement is available, the binary response results in the smallest area whereas the full response results in a wider span of pixels assigned the value of the measurement, compare the horizontal extents of the gray and red boxes in center and right panels of Fig. 31. Thus, in sparsely covered areas, being more compact the binary PSRF response can be thought of as having finer compared to the full response, but the full response may better fill in gaps between measurements.

In contrast, when multiple overlapping measurements are available, i.e., the surface is oversampled, it is possible to obtain images with finer effective resolution. This is seen by comparing the blue PSRFs in the center and right panels of Fig. 31. The multi measurement PSRF was computed by summing the MRFs of a dense set of measurements and then normalizing. This summation can be done in linear space (i.e., not in dB) or in dB. As noted in Section 5.3, the latter is used for SIR. The improvement in resolution (narrowing of the width) of the PSRF compared to the MRF is apparent.

Enhancement of the effective resolution *requires* dense sampling of the surface. This is the reason multiple passes are used. In addition, multiple measurements at a diversity of incidence angles are required to estimate the incidence angle slope. When the surface is adequately sampled, the effective spatial resolution is improved, which can result in a reduction in noise. However, when the surface is undersampled, it is difficult for the image resolution to be much better than the MRF resolution.

Because NSCAT had fewer HH-pol beams than VV-pol, the HH-pol images are frequently undersampled, particularly for 4-day images made separately for morning and evening intervals. Undersampling is less frequent for 8-day images, particularly for the "B" all pass case. To illustrate the effects that MRF choice has on the resulting images when the surface is undersampled, consider Figs. 32 and 33. Figure 32 shows an 8-day "both" HH-pol image which is much more densely sampled than the 4-day evening image in Fig. 33 that compares binary and full response SIR images. Note the difference in the areas covered between different MRFs in the 4-day images. While the full response MRF better covers the surface, it also leads to herring-bone patterns in the image that are evident in the left center of Greenland. These do not appear in the 8-day image in Figs. 32.

## 6.4 Data Volume

Table 5 summarizes available CETB *NSCAT* radar products, which are all in CETB-standard EASE-2 Grid projections. In this table, "days" refers to the length of time used for image formation. Imaging periods overlap, with a new image started each day. Note that for ltod images that in order to have the right number of morning or evening passes, the time period of the measurements actually used in the images may extend slightly outside the multi-day

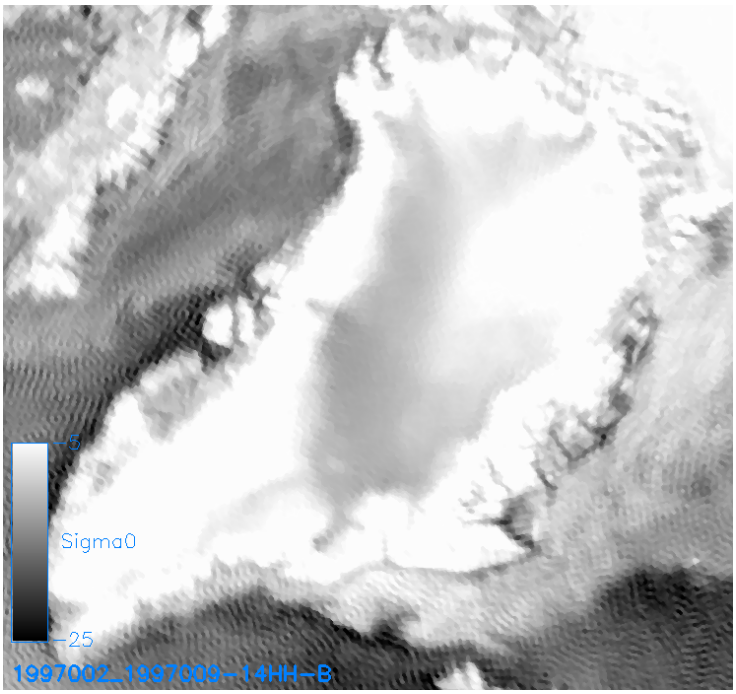


**Figure 32:** *Greenland 8-day HH pol "both" days 2-9, 1997 $\sigma^o$ at 40° computed assuming the full response MRF.*

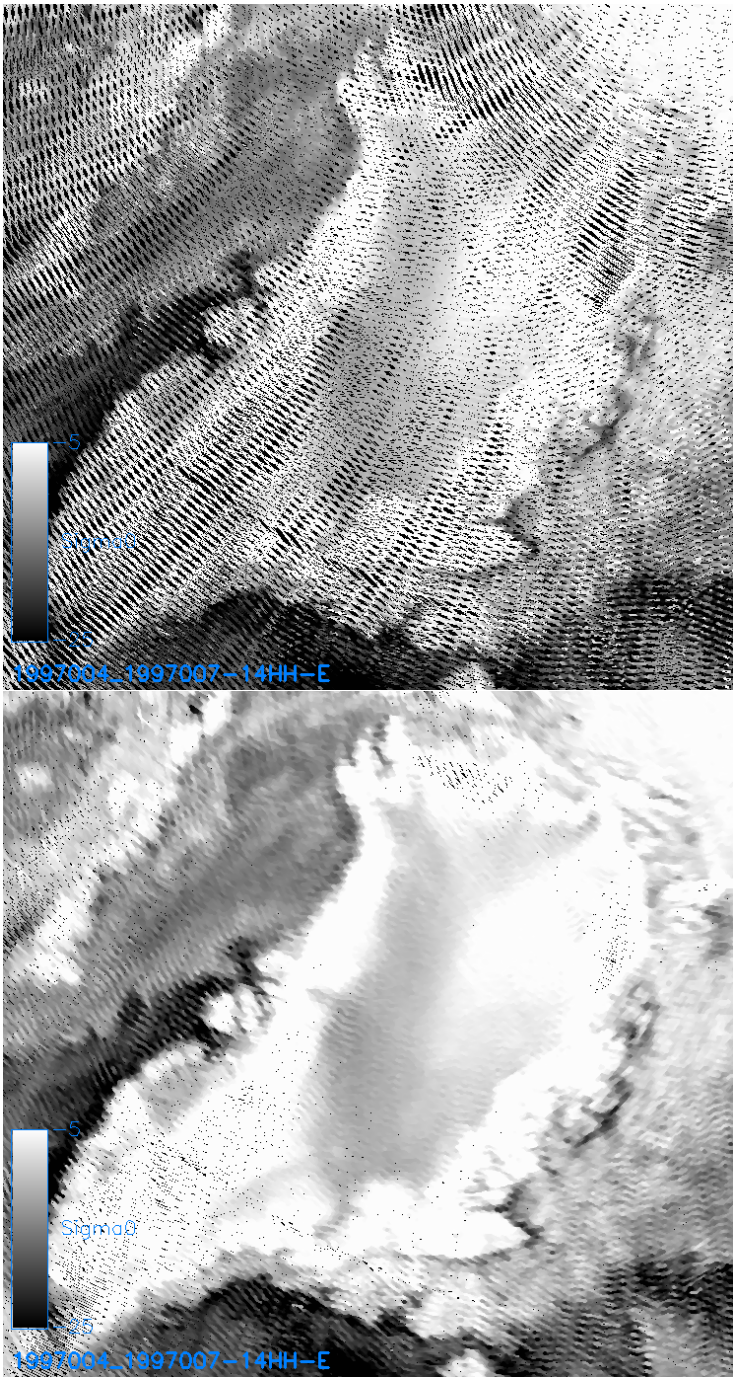


**Figure 33:** *Greenland 4-day HH pol evening SIR image days 4-7, 1997. The images are clearly undersampled. (top) $\sigma^o$ at 40° computed assuming a binary MRF. (bottom) $\sigma^o$ at 40° computed assuming the full response MRF.*

period. Individual file sizes vary due to internal file compression for each image type. See Section 4.5 for access details.

# 7 Acknowledgements

This work utilizes resources from the Brigham Young University Scatterometer Climate Record Pathfinder and University of Colorado Boulder Research Computing Group, which is supported by the National Science Foundation (awards TBD), the University of Colorado Boulder and Colorado State University.

# 8 References

# References

Ashcraft, I. S. and D. G. Long. 2006. Relating microwave backscatter azimuth modulation to surface properties of the Greenland ice sheet. *Journal of Glaciology 52*(177), 257–266. doi:10.3189/172756506781828764.

Brodzik, M. J., B. Billingsley, T. Haran, B. Raup, and M. H. Savoie. 2012. EASE-Grid 2.0: Incremental but significant improvements for Earth-gridded data sets. *International Society for Photogrammetry and Remote Sensing 1*, 32–45. doi:10.3390/ijgi101003.

Brodzik, M. J., B. Billingsley, T. Haran, B. Raup, and M. H. Savoie. 2014. Correction: Brodzik, M.J., *et al.* EASE-Grid 2.0: Incremental but Significant Improvements for Earth-Gridded Data Sets, *ISPRS Int. J. Geo-Inf.* 2012, 1, 32–45. *ISPRS Int. J. Geo-Inf. 3*, 1154–1156. doi:10.3390/ijgi3031154.

Brodzik, M. J. and K. Knowles. 2011. EASE-Grid 2.0 Land-Ocean-Coastline-Ice Masks Derived from Boston University MODIS/Terra Land Cover Data. NASA National Snow and Ice Data Center DAAC, Boulder, CO USA. Digital Media, http://nsidc.org/data/nsidc-0610, doi:https://doi.org/10.5067/XR8523MC24TB.

Brodzik, M. J., D. G. Long, M. A. Hardman, A. Paget, and R. L. Armstrong. 2016, updated 2021. MEaSUREs Calibrated Enhanced-Resolution Passive Microwave Daily EASE-Grid 2.0 Brightness Temperature ESDR, Version 1. National Snow and Ice Data Center, Boulder, CO USA. Digital Media, http://nsidc.org/data/nsidc-0630, doi:https://doi.org/10.5067/MEASURES/CRYOSPHERE/NSIDC-0630.001.

Brodzik, M. J., J. M. Ramage, M. A. Hardman, D. G. Long, and R. L. Armstrong. 2018. Improving melt onset detection in mountainous regions from the new, enhanced-resolution passive microwave climate record. Poster presentation at EGU General Assembly, CR 2.1:10690, Vienna, Austria, 9–13 April.

Early, D. S. and D. G. Long. 2001. Image reconstruction and enhanced resolution imaging from irregular samples. *IEEE Transactions on Geoscience and Remote Sensing 39*(2), 291–302. doi:10.1109/36.905237.

Faist, G. and W.-P. Lee. 1997. NASA Scatterometer (NSCAT) science data processing system Level 1.5 data software interface specification (SIS-2): 597-522-22, rev. D. JPL D-11788, Rev. D, Jet Propulsion Laboratory, Pasadena, CA.

Graf, J., C. Sasaki, C. Winn, W. Liu, W. Tsai, M. Freilich, and D. G. Long. 1998. NASA scatterometer experiment. *Acta Astronautica 43*(7-8), 377–407. doi:10.1016/S0094-5765(97)00180-X.

Grantham, W. L., E. M. Bracalente, W. L. Jones, and J. W. Johnson. 1977. The Seasat-A satellite scatterometer. *IEEE Journal of Oceanic Engineering OE-2*(2), 200–206.

JPL. 1997. NASA scatterometer science data product user's manual: Overview & geophysical data products: Version 1.1. JPL D-12985, Jet Propulsion Laboratory, Pasadena, CA.

Lindsley, R. and D. Long. 2016. ASCAT and QuikSCAT azimuth modulation of backscatter over East Antarctica. *IEEE Geoscience and Remote Sensing Letters, 13*(8), 1134–1138. doi:10.1109/LGRS.2016.2572101.

Long, D. and M. Brodzik. 2016a. Optimum image formation for spaceborne microwave radiometer products. *IEEE Trans. Geosci. Remote Sensing 54*(5), 2763–2779. doi:10.1109/TGARS.2015.2505677.

Long, D. and D. Daum. 1998. Spatial resolution enhancement of SSM/I data. *IEEE Trans. Geosci. Remote Sensing 36*(2), 407–417.

Long, D. and M. Drinkwater. 2000. Azimuth variation in microwave scatterometer and radiometer data over Antarctica. *IEEE Transactions on Geoscience and Remote Sensing 38*(4), 1857–1870. doi:10.1109/36.851769.

Long, D. and R. Franz. 2016a. Band-limited signal reconstruction from irregular samples with variable apertures. *IEEE Transactions on Geoscience and Remote Sensing 54*(4), 2424–2436. doi:10.1109/TGRS.2015.2501366.

Long, D., P. Hardin, and P. Whiting. 1993. Resolution enhancement of spaceborne scatterometer data. *IEEE Trans. Geosci. Remote Sensing 31*(3), 700–715. doi:10.1109/36.225536.

Long, D. G.. 2017. Comparison of SeaWinds backscatter imaging algorithms. *IEEE J. Sel. Topics in Applied Earth Observations 10*(3), 2214–2231. doi:10.1109/JSTARS.2016.2626966.

Long, D. G. and M. J. Brodzik. 2016b, May. Optimum Image Formation for Spaceborne Microwave Radiometer Products. *IEEE Transactions on Geoscience and Remote Sensing 54*(5), 2763–2779. doi:10.1109/TGRS.2015.2505677.

Long, D. G., M. J. Brodzik, and M. A. Hardman. 2019. Enhanced–Resolution SMAP Brightness Temperature Image Products. *IEEE Transactions on Geoscience and Remote Sensing 57*(7), 4151–4163. doi:10.1109/TGRS.2018.2889427.

Long, D. G., C.-Y. Chi, and F. K. Li. 1988. The design of an onboard digital doppler processor for a spaceborne scatterometer. *IEEE Transactions on Geoscience and Remote Sensing 26*(6), 869–878. doi:10.1109/36.7718.

Long, D. G. and M. R. Drinkwater. 1994. Greenland ice-sheet surface properties observed by the Seasat-A scatterometer at enhanced resolution. *IEEE Transactions on Geoscience and Remote Sensing 40*(135), 213–230.

Long, D. G. and R. O. W. Franz. 2016b. Band–limited Signal Reconstruction from Irregular Samples with Variable Apertures. *IEEE Transactions on Geoscience and Remote Sensing 54*(4), 2424–2436. doi:10.1109/TGRS.2015.2501366.

Meissner, T., L. Ricciardulli, and F. J. Wentz. 2017. Capability of the SMAP mission to measure ocean surface winds in storms. *Bulletin of the American Meteorological Society 98*(8), 1660–1677. doi:10.1175/BAMS-D-16-0052.1.

Naderi, F., M. H. Freilich, and D. G. Long. 1991. Spaceborne radar measurement of wind velocity over the ocean–an overview of the NSCAT scatterometer system. *Proceedings of the IEEE 79*(6), 850–866. doi:10.1109/5.90163.

Pitas, I. and A. Venetsanopoulos. 1986. Nonlinear mean filters in image processing. *IEEE Transactions on Acoustics, Speech, and Signal Processing 34*(3), 573–584. doi:10.1109/TASSP.1986.1164857.

Stephen, H. and D. G. Long. 2007. Spatial and temporal behavior of microwave backscatter directional modulation over the Saharan ergs. *IEEE Transactions on Geoscience and Remote Sensing 45*(5), 1164–1173. doi:10.1109/TGRS.2007.892584.

Tsai, W.-Y., J. E. Graf, C. Winn, J. N. Huddleston, S. Dunbar, M. H. Freilich, F. J. Wentz, D. G. Long, and W. Jones. 1999. Postlaunch sensor verification and calibration of the NASA Scatterometer. *IEEE Transactions on Geoscience and Remote Sensing 37*(3), 1517–1542. doi:10.1109/36.763264.

Ulaby, F. T. and D. G. Long. 2014. *Microwave Radar and Radiometric Remote Sensing*. Ann Arbor, MI, USA: University of Michigan Press.

Wikipedia. visited 8 Oct. 2016. Geometric mean. Online, http://en.wikipedia.org/wiki/Geometric_mean.

# Appendices

## A *NSCAT* Projections and Grids

**Table 7:** NSCAT *25 km product EASE-Grid 2.0 projections and grid dimensions, produced for compatibility with CETB ESDR data products (Brodzik et al., 2021)*.

| Name | Projection | Resolution (km) | Cols | Rows | Latitude Extent | Longitude Extent |
|---|---|---|---|---|---|---|
| EASE2-T25km | Temperate and Tropical Cylindrical | 25.025 260 00 | 1388 | 540 | ±67.057 640 6° | ±180° |
| EASE2-T3.125km | Temperate and Tropical Cylindrical | 3.128 157 50 | 11 104 | 4320 | ±67.057 640 6° | ±180° |
| EASE2-N25km | Northern Lambert Azimuthal | 25.0 | 720 | 720 | 0°–90° | ±180° |
| EASE2-N3.125km | Northern Lambert Azimuthal | 3.125 | 5760 | 5760 | 0°–90° | ±180° |
| EASE2-S25km | Southern Lambert Azimuthal | 25.0 | 720 | 720 | −90°–0° | ±180° |
| EASE2-S3.125km | Southern Lambert Azimuthal | 3.125 | 5760 | 5760 | −90°–0° | ±180° |

# B *NSCAT* Data Definition

## B.1 File Requirements

Following Brodzik et al. (2021), *NSCAT* product file requirements include:

- Output file format shall be acceptable for NSIDC DAAC to easily ingest to ECS
- File size maximum will be $< 1\,\mathrm{GB}$ (larger files are allowed in ECS, but fast network speeds cannot always be assumed)
- Files will conform to netCDF-CF 1.6 conventions for all but the requirement that puts the lat/lon arrays into the file; however, we will include CF-compliant coordinate variables with projected coordinate locations
- Files should pass CF-compliance-checking for all but the lat/lon arrays (we used JPL compliance-checker)
- Each file will contain 1 or more array variables, with associated ancillary variables, possibly different ancillary variables for each gridding technique. We may have a practical limit on the number of ancillary variables to include, limited by maximum file size
- Each file of the same type (GRD or SIR) will contain the same file-level metadata for that type.
- We will follow the DRY (Don't Repeat Yourself) principle: Metadata will not be duplicated at multiple places in the same file
- DRY exception: Time values will be machine- and human-readable
- DRY exception: Some projection metadata may be in multiple forms (a proj4 string and/or a WKT string)
- Variable/attribute names will be CF-compliant whenever possible

The *NSCAT* .nc files work with gdal utility, *gdal_translate*, to produce a geoTIFF version of each of the data variables <variable_name> in the file, (details in Brodzik et al. (2018)), for e.g.:

```
$ gdal_translate -of GTiff -b 1 \
NETCDF:''cetb.nc'':<variable_name> variable_name.tif
```

## B.2 Filename Convention

*NSCAT* data are distributed by the NSIDC DAAC (http://nsidc.org/data/nsidc-TBD).
Filenames are:
<product_id>-<grid_name>-<platform_sensor>-<yyyyddd>_<yyyyddd> -<channel_id>-<pass>-<algorithm>-<input_source>-<version>.nc
where parts of the filename are described in Table 8.

**Table 8:** NSCAT *file naming convention*

| Part | Description | Values |
|---|---|---|
| <product_id> | NSIDC unique data product id | NSIDC-TBD |
| <grid_name> | EASE-Grid 2.0 grid id | See Table 7 |
| <platform> | Satellite platform | ADEOS |
| <sensor> | Sensor name | NSCAT |
| <yyyyddd> | start date | 4-digit year and 3-digit day-of-year |
| <yyyyddd> | end date | 4-digit year and 3-digit day-of-year |
| <channel_id> | Channel (frequency in GHz and polarization) | 14 followed by polarization, one of:<br>• HH = horizontal-horizontal<br>• VV = vertical-vertical |
| <pass> | Pass direction (T grids) or ltod (N or S grids) | one of:<br>• B = Both (all measurements)<br>• A = Ascending<br>• D = Descending<br>• M = Morning<br>• E = Evening |
| <algorithm> | Reconstruction algorithm | one of GRD, AVE or SIR |
| <version> | Version number | production version number |

## B.3 File Content, v1.0

The following is a sample NetCDF *ncdump –h* utility output for a *NSCAT* v1.0 3.125 km SIR file. File-level metadata and processing details vary depending on projection, spatial resolution and processing details (method, input file list, etc.).

```
netcdf BYU-NSCAT-EASE2_S3.125km-ADEOS_NSCAT-1997119_1997126-14VV-M-SIR-v1.0 {
dimensions:
time = UNLIMITED ; // (1 currently)
y = 5760 ;
x = 5760 ;
variables:
double time(time) ;
time:standard_name = "time" ;
time:coverage_content_type = "coordinate" ;
```

```
time:long_name = "ANSI date" ;
time:units = "days since 1972-01-01 00:00:00" ;
time:calendar = "gregorian" ;
time:axis = "T" ;
time:valid_range = 0., 1.79769313486232e+308 ;
double y(y) ;
y:standard_name = "projection_y_coordinate" ;
y:coverage_content_type = "coordinate" ;
y:long_name = "y" ;
y:units = "meters" ;
y:axis = "Y" ;
y:valid_range = -9000000., 9000000. ;
double x(x) ;
x:standard_name = "projection_x_coordinate" ;
x:coverage_content_type = "coordinate" ;
x:long_name = "x" ;
x:units = "meters" ;
x:axis = "X" ;
x:valid_range = -9000000., 9000000. ;
char crs ;
crs:grid_mapping_name = "lambert_azimuthal_equal_area" ;
crs:longitude_of_projection_origin = 0. ;
crs:latitude_of_projection_origin = -90. ;
crs:false_easting = 0. ;
crs:false_northing = 0. ;
crs:semi_major_axis = 6378137. ;
crs:inverse_flattening = 298.257223563 ;
crs:proj4text = "+proj=laea +lat_0=-90 +lon_0=0 +x_0=0 +y_0=0 +ellps=WGS84 +datum=WGS84
crs:srid = "urn:ogc:def:crs:EPSG::6932" ;
crs:coverage_content_type = "auxiliaryInformation" ;
crs:references = "[\"EASE-Grid 2.0 documentation: http://nsidc.org/data/ease/ease_grid2.
crs:crs_wkt = "PROJCRS[\"WGS 84 / NSIDC EASE-Grid 2.0 South\", BASEGEODCRS[\"WGS 84\", D
crs:long_name = "EASE2_S3.125km" ;
short Sigma0_ave(time, y, x) ;
Sigma0_ave:standard_name = "brightness_temperature" ;
Sigma0_ave:long_name = "SIR Sigma0" ;
Sigma0_ave:units = "1" ;
Sigma0_ave:_FillValue = -32768s ;
Sigma0_ave:valid_range = 0s, 32767s ;
Sigma0_ave:packing_convention = "netCDF" ;
```

```
Sigma0_ave:packing_convention_description = "unpacked = scale_factor*packed + add_offset
Sigma0_ave:scale_factor = 0.002f ;
Sigma0_ave:add_offset = -55.f ;
Sigma0_ave:grid_mapping = "crs" ;
Sigma0_ave:coverage_content_type = "image" ;
short Sigma0_slope_ave(time, y, x) ;
Sigma0_slope_ave:standard_name = "brightness_temperature" ;
Sigma0_slope_ave:long_name = "SIR Sigma0 slope" ;
Sigma0_slope_ave:units = "1" ;
Sigma0_slope_ave:_FillValue = -32768s ;
Sigma0_slope_ave:valid_range = 0s, 32767s ;
Sigma0_slope_ave:packing_convention = "netCDF" ;
Sigma0_slope_ave:packing_convention_description = "unpacked = scale_factor*packed + add_
Sigma0_slope_ave:scale_factor = 0.001f ;
Sigma0_slope_ave:add_offset = -2.f ;
Sigma0_slope_ave:grid_mapping = "crs" ;
Sigma0_slope_ave:coverage_content_type = "image" ;
short Sigma0(time, y, x) ;
Sigma0:standard_name = "brightness_temperature" ;
Sigma0:long_name = "SIR Sigma0" ;
Sigma0:units = "1" ;
Sigma0:_FillValue = -32768s ;
Sigma0:valid_range = 0s, 32767s ;
Sigma0:packing_convention = "netCDF" ;
Sigma0:packing_convention_description = "unpacked = scale_factor*packed + add_offset" ;
Sigma0:scale_factor = 0.002f ;
Sigma0:add_offset = -55.f ;
Sigma0:grid_mapping = "crs" ;
Sigma0:coverage_content_type = "image" ;
Sigma0:sir_number_of_iterations = 30 ;
Sigma0:median_filter = 1 ;
Sigma0:temporal_division = "Morning" ;
Sigma0:temporal_division_local_start_time = 5.f ;
Sigma0:temporal_division_local_end_time = 17.f ;
Sigma0:frequency_and_polarization = "14VV" ;
short Sigma0_slope(time, y, x) ;
Sigma0_slope:standard_name = "brightness_temperature" ;
Sigma0_slope:long_name = "SIR Sigma0 slope" ;
Sigma0_slope:units = "1" ;
Sigma0_slope:_FillValue = -32768s ;
```

```
Sigma0_slope:valid_range = 0s, 32767s ;
Sigma0_slope:packing_convention = "netCDF" ;
Sigma0_slope:packing_convention_description = "unpacked = scale_factor*packed + add_offs
Sigma0_slope:scale_factor = 0.001f ;
Sigma0_slope:add_offset = -2.f ;
Sigma0_slope:grid_mapping = "crs" ;
Sigma0_slope:coverage_content_type = "image" ;
short Sigma0_num_samples(time, y, x) ;
Sigma0_num_samples:long_name = "SIR Number of Measurements" ;
Sigma0_num_samples:units = "count" ;
Sigma0_num_samples:_FillValue = 0s ;
Sigma0_num_samples:valid_range = 1s, 255s ;
Sigma0_num_samples:grid_mapping = "crs" ;
Sigma0_num_samples:coverage_content_type = "auxiliaryInformation" ;
short Incidence_angle(time, y, x) ;
Incidence_angle:standard_name = "angle_of_incidence" ;
Incidence_angle:long_name = "SIR Incidence Angle" ;
Incidence_angle:units = "degree" ;
Incidence_angle:_FillValue = -1s ;
Incidence_angle:valid_range = 0s, 9000s ;
Incidence_angle:packing_convention = "netCDF" ;
Incidence_angle:packing_convention_description = "unpacked = scale_factor*packed + add_o
Incidence_angle:scale_factor = 0.01f ;
Incidence_angle:add_offset = 0.f ;
Incidence_angle:grid_mapping = "crs" ;
Incidence_angle:coverage_content_type = "auxiliaryInformation" ;
short Sigma0_std_dev(time, y, x) ;
Sigma0_std_dev:long_name = "SIR Sigma0 standard deviation" ;
Sigma0_std_dev:units = "1" ;
Sigma0_std_dev:_FillValue = -32768s ;
Sigma0_std_dev:valid_range = -32766s, 32767s ;
Sigma0_std_dev:packing_convention = "netCDF" ;
Sigma0_std_dev:packing_convention_description = "unpacked = scale_factor*packed + add_of
Sigma0_std_dev:scale_factor = 0.002f ;
Sigma0_std_dev:add_offset = 0.f ;
Sigma0_std_dev:grid_mapping = "crs" ;
Sigma0_std_dev:coverage_content_type = "auxiliaryInformation" ;
short Sigma0_time(time, y, x) ;
Sigma0_time:long_name = "Time of Day" ;
Sigma0_time:units = "minutes since 1997-04-29 00:00:00" ;
```

```
Sigma0_time:_FillValue = -32768s ;
Sigma0_time:valid_range = -32767s, 32767s ;
Sigma0_time:packing_convention = "netCDF" ;
Sigma0_time:packing_convention_description = "unpacked = scale_factor*packed + add_offse
Sigma0_time:scale_factor = 1.f ;
Sigma0_time:add_offset = 0.f ;
Sigma0_time:grid_mapping = "crs" ;
Sigma0_time:coverage_content_type = "auxiliaryInformation" ;
Sigma0_time:calendar = "gregorian" ;

// global attributes:
:references = "Early, D. S., and D.G. Long. 2001. Image Reconstruction and Enhanced Reso
:title = "NSCAT Radar Twice-Daily SIRF-Enhanced EASE-Grid 2.0 Sigma0" ;
:id = "doi:10.5067/APSWI5NK3PKJ" ;
:summary = "Enhanced-resolution, gridded NSCAT Ku-band radar backscatter" ;
:project = "Scatterometer Climate Record Pathfinder" ;
:contributor_name = "David G. Long, NASA Scatterometer Climate Record Pathfinder" ;
:contributor_role = "Principal Investigator and Developer, Data Producer" ;
:citation = "D. G. Long\nNSCAT Twice-Daily SIRF-Enhanced EASE-Grid 2.0 Sigma0.\nVersion
:license = "These data are freely, openly, and fully available to use without\nrestricti
:Conventions = "CF-1.6, ACDD-1.3" ;
:product_version = "v1.0" ;
:software_version_id = "1.0.0" ;
:software_repository = "" ;
:history = "nscat_meta_sir_cetb" ;
:comment = "Epoch date for data in this file: 1997-04-29 00:00:00Z" ;
:source = "doi:TBD (NSCAT L1.5 data): See input_fileN list and number_of_input_files att
:metadata_link = "http://www.scp.byu.edu/" ;
:institution = "Scatterometer Climate Record Pathfinder\nElectrical and Computer Enginee
:publisher_name = "Scatterometer Climate Record Pathfinder" ;
:publisher_type = "institution" ;
:publisher_url = "http://www.scp.byu.edu" ;
:publisher_email = "long@ee.byu.edu" ;
:program = "NASA Earth Science Data and Information System (ESDIS)" ;
:standard_name_vocabulary = "CF Standard Name Table (v27, 28 September 2013)" ;
:cdm_data_type = "Grid" ;
:keywords = "EARTH SCIENCE > SPECTRAL/ENGINEERING > MICROWAVE > RADAR BACKSCATTER" ;
:keywords_vocabulary = "NASA Global Change Master Directory (GCMD) Earth Science Keyword
:platform = "NSCAT > NASA Scatterometer on ADEOS" ;
:platform_vocabulary = "NASA Global Change Master Directory (GCMD) Earth Science Keyword
```

```
:instrument = "NSCAT Ku-BAND RADAR > NSCAT Ku-Band Radar" ;
:instrument_vocabulary = "NASA Global Change Master Directory (GCMD) Earth Science Keywo
:time_coverage_resolution = "P1d" ;
:geospatial_bounds = "" ;
:geospatial_bounds_crs = "" ;
:geospatial_x_units = "meters" ;
:geospatial_y_units = "meters" ;
:naming_authority = "org.doi.dx" ;
:date_created = "2022-12-31T06:57:46GMT" ;
:date_modified = "2022-12-31T06:57:46GMT" ;
:date_issued = "2022-12-31T06:57:46GMT" ;
:date_metadata_modified = "2022-12-31T06:57:46GMT" ;
:input_data_quality_filtering = "Only used highest-quality input data." ;
:acknowledgement = "This data set was created with funding from NASA Grant #TBD." ;
:processing_level = "Level 3" ;
:creator_name = "David Long" ;
:creator_type = "person" ;
:creator_email = "long@ee.byu.edu" ;
:creator_url = "http://www.scp.byu.edu" ;
:creator_institution = "Electrical and Computer Engineering Department\nBrigham Young Un
:geospatial_lat_min = -90. ;
:geospatial_lat_max = 0. ;
:geospatial_lon_min = -180. ;
:geospatial_lon_max = 180. ;
:geospatial_lat_units = "degrees_north" ;
:geospatial_lon_units = "degrees_east" ;
:geospatial_x_resolution = "3125.00 meters" ;
:geospatial_y_resolution = "3125.00 meters" ;
:time_coverage_start = "1997-04-06T06:54:00.00Z" ;
:time_coverage_end = "1997-05-21T17:02:00.00Z" ;
:time_coverage_duration = "P45T10:08:00.00" ;
:number_of_input_files = 115 ;
:input_file1 = "S1503637.DAT" ;
:input_file2 = "S1503638.DAT" ;
:input_file3 = "S1503639.DAT" ;
:input_file4 = "S1503640.DAT" ;
:input_file5 = "S1503641.DAT" ;
:input_file6 = "S1503642.DAT" ;
:input_file7 = "S1503643.DAT" ;
:input_file8 = "S1503644.DAT" ;
```

```
:input_file9 = "S1503645.DAT" ;
:input_file10 = "S1503646.DAT" ;
:input_file11 = "S1503647.DAT" ;
:input_file12 = "S1503648.DAT" ;
:input_file13 = "S1503649.DAT" ;
:input_file14 = "S1503650.DAT" ;
:input_file15 = "S1503651.DAT" ;
:input_file16 = "S1503652.DAT" ;
:input_file17 = "S1503653.DAT" ;
:input_file18 = "S1503654.DAT" ;
:input_file19 = "S1503655.DAT" ;
:input_file20 = "S1503656.DAT" ;
:input_file21 = "S1503657.DAT" ;
:input_file22 = "S1503658.DAT" ;
:input_file23 = "S1503659.DAT" ;
:input_file24 = "S1503660.DAT" ;
:input_file25 = "S1503661.DAT" ;
:input_file26 = "S1503662.DAT" ;
:input_file27 = "S1503663.DAT" ;
:input_file28 = "S1503664.DAT" ;
:input_file29 = "S1503665.DAT" ;
:input_file30 = "S1503666.DAT" ;
:input_file31 = "S1503667.DAT" ;
:input_file32 = "S1503668.DAT" ;
:input_file33 = "S1503669.DAT" ;
:input_file34 = "S1503670.DAT" ;
:input_file35 = "S1503671.DAT" ;
:input_file36 = "S1503672.DAT" ;
:input_file37 = "S1503673.DAT" ;
:input_file38 = "S1503674.DAT" ;
:input_file39 = "S1503675.DAT" ;
:input_file40 = "S1503676.DAT" ;
:input_file41 = "S1503677.DAT" ;
:input_file42 = "S1503678.DAT" ;
:input_file43 = "S1503679.DAT" ;
:input_file44 = "S1503680.DAT" ;
:input_file45 = "S1503681.DAT" ;
:input_file46 = "S1503682.DAT" ;
:input_file47 = "S1503683.DAT" ;
:input_file48 = "S1503684.DAT" ;
```

```
:input_file49 = "S1503685.DAT" ;
:input_file50 = "S1503686.DAT" ;
:input_file51 = "S1503687.DAT" ;
:input_file52 = "S1503688.DAT" ;
:input_file53 = "S1503689.DAT" ;
:input_file54 = "S1503690.DAT" ;
:input_file55 = "S1503691.DAT" ;
:input_file56 = "S1503692.DAT" ;
:input_file57 = "S1503693.DAT" ;
:input_file58 = "S1503694.DAT" ;
:input_file59 = "S1503695.DAT" ;
:input_file60 = "S1503696.DAT" ;
:input_file61 = "S1503697.DAT" ;
:input_file62 = "S1503698.DAT" ;
:input_file63 = "S1503699.DAT" ;
:input_file64 = "S1503700.DAT" ;
:input_file65 = "S1503701.DAT" ;
:input_file66 = "S1503702.DAT" ;
:input_file67 = "S1503703.DAT" ;
:input_file68 = "S1503704.DAT" ;
:input_file69 = "S1503705.DAT" ;
:input_file70 = "S1503706.DAT" ;
:input_file71 = "S1503707.DAT" ;
:input_file72 = "S1503708.DAT" ;
:input_file73 = "S1503709.DAT" ;
:input_file74 = "S1503710.DAT" ;
:input_file75 = "S1503711.DAT" ;
:input_file76 = "S1503712.DAT" ;
:input_file77 = "S1503713.DAT" ;
:input_file78 = "S1503714.DAT" ;
:input_file79 = "S1503715.DAT" ;
:input_file80 = "S1503716.DAT" ;
:input_file81 = "S1503717.DAT" ;
:input_file82 = "S1503718.DAT" ;
:input_file83 = "S1503719.DAT" ;
:input_file84 = "S1503720.DAT" ;
:input_file85 = "S1503721.DAT" ;
:input_file86 = "S1503722.DAT" ;
:input_file87 = "S1503723.DAT" ;
:input_file88 = "S1503724.DAT" ;
```

```
:input_file89 = "S1503725.DAT" ;
:input_file90 = "S1503726.DAT" ;
:input_file91 = "S1503727.DAT" ;
:input_file92 = "S1503728.DAT" ;
:input_file93 = "S1503729.DAT" ;
:input_file94 = "S1503730.DAT" ;
:input_file95 = "S1503731.DAT" ;
:input_file96 = "S1503732.DAT" ;
:input_file97 = "S1503733.DAT" ;
:input_file98 = "S1503734.DAT" ;
:input_file99 = "S1503735.DAT" ;
:input_file100 = "S1503736.DAT" ;
:input_file101 = "S1503737.DAT" ;
:input_file102 = "S1503738.DAT" ;
:input_file103 = "S1503739.DAT" ;
:input_file104 = "S1503740.DAT" ;
:input_file105 = "S1503741.DAT" ;
:input_file106 = "S1503742.DAT" ;
:input_file107 = "S1503743.DAT" ;
:input_file108 = "S1503744.DAT" ;
:input_file109 = "S1503745.DAT" ;
:input_file110 = "S1503746.DAT" ;
:input_file111 = "S1503747.DAT" ;
:input_file112 = "S1503748.DAT" ;
:input_file113 = "S1503749.DAT" ;
:input_file114 = "S1503750.DAT" ;
:input_file115 = "S1503751.DAT" ;
}
```